QUANTITATIVE MEASUREMENT OF THE DENSITY GRADIENT FIELD IN A NORMAL IMPEDANCE TUBE USING AN OPTICAL DEFLECTOMETER

By

PRIYA NARAYANAN

A THESIS PRESENTED TO THE GRADUATE SCHOOL
OF THE UNIVERSITY OF FLORIDA IN PARTIAL FULFILLMENT
OF THE REQUIREMENTS FOR THE DEGREE OF
MASTER OF SCIENCE

UNIVERSITY OF FLORIDA

2003

ACKNOWLEDGMENTS

I would like to thank foremost my advisor, Dr. Louis N Cattafesta, for his guidance, support and patience. His continual guidance and motivation made this work possible. I would also like to express my heartfelt gratitude to my co-advisor Dr. Mark Sheplak for his support.

I owe special thanks to Dr. Bruce Caroll and Dr. Paul Hubner for their help during the design of the experimental set-up. I thank all of the students in the Interdisciplinary Microsystems Group, particularly Ryan Holman, for his help during data acquisition. I would also like to express my gratitude to my colleagues Todd Schultz, Steve Horowitz, Anurag Kasyap, Karthik Kadirvel and David Martin for their help during the course of this project.

I would like to thank my undergraduate advisor Dr. Job Kurian for his motivation and encouragement. I would also like to thank my roommates and friends for making my stay in Gainesville a memorable one. Finally, I want to thank my parents and my sister Poornima for their endless support.

TABLE OF CONTENTS

page

ACKNOWLEDGMENTS iii

LIST OF TABLES vi

LIST OF FIGURES vii

ABSTRACT x

1 INTRODUCTION 1

1.1 Basic Schlieren Method 2
1.2 Optical Deflectometer 5
1.3 Review of an Optical Deflectometer 5
1.4 Research Objectives 8
1.5 Thesis Outline 9

2 OPTICAL DEFLECTOMETER 10

2.1 Normal Impedance Tube 10
2.2 Theory of a Schlieren System 13
2.2.1 Deflection of Light by a Density Gradient 14
2.2.2 The Toepler Method 16
2.3 Sensitivity Analysis 20

3 EXPERIMENTAL SET UP 27

3.1 Basic Schlieren Setup 27
3.2 Normal Impedance Tube 28
3.2.1 Components 28
3.2.2 Fabrication of the Test Section 29
3.3 Data Acquisition System 30
3.3.1 Photosensor Module 31
3.3.2 Positioning System 31
3.3.3 Signal-Processing Equipment 31

4 DATA ANALYSIS 32

4.1 Calibration of the Optical Deflectometer 32
4.2 Data Reduction Procedure 41

4.3 Dynamic Calibration 45
4.4 Experimental Procedure 47

5 RESULTS AND DISCUSSION 49

5.1 Theoretical Results 49
5.2 Numerical Results 52
5.3 Experimental Results 55
5.3.1 Measurement of Density Gradient Using the Optical Deflectometer 55
5.3.2 Measurement of Density Gradient Using microphones 63
5.3.3 Comparison of Results Obtained by the Two Methods 65

6 CONCLUSION AND FUTURE WORK 69

6.1 Conclusions 69
6.2 Future Work 69

APPENDIX

A KNIFE-EDGE GEOMETRY 71

B LIGHT RAYS IN AN INHOMOGENEOUS FLUID 73

C UNCERTAINTY ANALYSIS 75

C.1 Uncertainty in Amplitude 75
C.1.1 Deflectometer Method 75
C.1.1 Two Microphone Method 79
C.2 Uncertainty in Phase 82
C.2.1 Deflectometer Method 82
C.2.2 Microphone method 84

D DENSITY GRADIENT 85

LIST OF REFERENCES 87

BIOGRAPHICAL SKETCH 89

LIST OF TABLES

Table page

4-1 Slope of the calibration curve at three different locations.....40

C-1 Uncertainties in various parameters for a deflectometer.....78

C-2 Uncertainties in various parameters for the microphone method.....80

LIST OF FIGURES

Figure page

1-1 Simple schlieren setup. 4

2-1 Plane wave tube. 11

2-2 Light source in the plane of the knife-edge 18

2-3 Ray diagram of the schlieren setup. 21

2-4 Schlieren head with the conjugate plane. 25

3-1 Deflectometer set-up. 28

3-2 Normal impedance tube 29

3-3 Setup for normal impedance tube. 30

4-1 Light source in the plane of the knife-edge. 33

4-2 Knife-edge calibration of photodiode sensor. 36

4-3 Photodiode knife-edge calibration. 37

4-4 Photodiode knife-edge calibrations at three locations. 38

4-5 Linear region of the calibration curves at three locations after regression analysis. 39

4-6 Calibration curves after the ground glass was inserted. 40

4-7 Slope of the calibration curve plotted along the test section. 40

4-8 Data reduction procedure. 44

4-9 Impulse response of the experimental photo-detector. 45

4-10 Frequency response of the experimental photo-detector at the experimental gain setting. 46

5-1 Comparison of pressure, density and density gradient distributions. 50

5-2 Phase variation for a rigid termination. 51

5-3 Pressure waves at various phases for R = 1. 53

5-4 Pressure waves at various phases for R = 0. 53

5-5 Pressure waves at various phases for R = 0.5. 54

5-6 Noise floor of the experimental photo-detector at an operational gain of 0.35 56

5-7 Noise floor of the experimental photo-detector (light-on) for various gains. 56

5-8 Example of photo-detector power spectrum at 145.4 dB 57

5-9 Example of reference microphone power spectrum at 145.4 dB 57

5-10 Example of coherent spectrum at 145.4 dB 58

5-11 Example of photo-detector coherence power at 145.4 dB 58

5-12 Magnitude of the frequency response function at 145.4 dB 59

5-13 Density gradient amplitude along the length of the tube at 145.4 dB 59

5-14 Example of photo-detector power spectrum at 126.4 dB 60

5-15 Example of reference microphone power spectrum at 126.4 dB 61

5-16 Coherent power of the photo-detector at 126.4 dB 61

5-17 Example of coherence spectrum at 126.4 dB 62

5-18 Density gradient amplitude along the length of the tube at 126.4 dB 62

5-19 Phase difference between the photo-detector signal and the reference microphone signal at 145.4 dB 63

5-20 Density gradient amplitude along the length of the tube using the microphone method at 145.4 dB 64

5-21 Density gradient phase along the length of the tube using the microphone method at 145.4 dB 64

5-22 Magnitude of the density gradient using the two methods at 145.4 dB 65

5-23 Magnitude of the density gradient using the two methods at 126.4 dB 66

5-24 Phase of the density gradient using the two methods at 145.4 dB 67

5-25 Phase of the density gradient using the two methods at 145.4 dB after the phase correction from the photo detector. 67

5-26 Phase of the density gradient using the two methods at 126.4 dB after the phase correction from the photo detector. 68

A-1 Magnification of the source on the screen. 71

B-1 Deflection of a light ray in inhomogeneous test object. 73

C-1 Error bar in the amplitude of the density gradient using the deflectometer at 145.4 dB 77

C-2 Error bar in the amplitude using the microphone method 145.4 dB 81

C-3 Comparison of microphone and deflectometer method at 145.4 dB 81

C-4 Error bar in the phase using the deflectometer at 145.4 dB 82

C-6 Error bar in the amplitude using the deflectometer at 145.4 dB 83

C-7 Comparison of microphone and deflectometer method at 145.4 dB 84

Abstract of Thesis Presented to the Graduate School
of the University of Florida in Partial Fulfillment of the
Requirements for the Degree of Master of Science

QUANTITATIVE MEASUREMENT OF DENSITY GRADIENT FIELD IN A NORMAL IMPEDANCE TUBE USING AN OPTICAL DEFLECTOMETER

By

Priya Narayanan

December 2003

Chair: Louis N. Cattafesta
Cochair: Mark Sheplak
Department: Mechanical and Aerospace Engineering

Interest is growing in optical flow-visualization techniques because they are inherently nonintrusive. A commonly used optical flow visualization technique is the schlieren method. This technique normally provides a qualitative measure of the density gradient by visualizing changes in refractive index that accompany the density changes in a flowfield. The "optical deflectometer" instrument extends the schlieren technique to quantitatively measure the density gradient. The optical deflectometer has been successfully used to characterize highly compressible flows. In this thesis, an optical deflectometer is studied that can provide quantitative measurements of the acoustic field in a normal impedance tube.

Results of the static calibration performed on the instrument are presented. The frequency response of the instrument is inferred using a laser impulse response test. Two-point cross-spectral analysis between the light intensity fluctuations in a schlieren

image and a reference microphone signal are used to determine the density gradient field in the normal impedance tube. Numerical simulations were obtained for test cases to validate the data-reduction method. In addition, the two-microphone method is used to verify the results obtained from the deflectometer.

Results of the experiments performed for normal sound pressure levels of $145.4\ dB$ and $126.4\ dB$ for a plane wave at $5\ kHz$ are presented. A detailed uncertainty analysis is also performed. The results were in good agreement with each other except at the density gradient maxima (pressure minima) at the higher sound pressure level.

.

CHAPTER 1
INTRODUCTION

Many modern-day research activities involve studies of substances that are colorless and transparent. The flow and temperature distribution [1] of many of these substances are of significant importance (for example, mixing of gases and liquids, convective heat transfer, plasma flow).

As suggested by the proverb "Seeing is believing," suggests, visualization is one of the best ways to understand the physics of any flow. Visualization also aids flow modeling. Hence, over the years numerous techniques have been developed to visualize the motion of fluids. These flow visualization techniques [2] have been used extensively in the field of engineering, physics, medical science, and oceanography .

In aerospace engineering, flow visualization has been an important tool in the field of fluid dynamics. Several flow visualization techniques [3] have been used in the study of flow past an airfoil, jet mixing in supersonic flows and acoustic oscillations.

Flow visualization can be classified as non-optical and optical techniques. In the former, seed particles are usually added and their motion observed. This indirectly gives information about the motion of the fluid itself. However, in the case of unsteady flow, these methods [2] are prone to error because of the finite size of the seed particles. Purely optical techniques, on the other hand, are based on the interaction of light rays with fluid flow in the absence of macroscopic seed particles. The information recorded is dependent on the change in optical properties of the fluid. One of the commonly studied properties is the variation in refractive index with fluid flow.

Several methods are commonly used to visualize refractive-index variation in fluids. Common methods [3] include shadowgraph, schlieren and interferometric techniques. Since these techniques are non-intrusive, the flow is not disturbed by the measurement technique.

Classical optical flow visualization tools (like schlieren and shadowgraphy) were used in the study of compressible or high-density gradient flows [2] (shock waves in wind tunnels, turbulent flow, convection patterns in liquids, etc.) Many of these techniques have been extended for the quantitative study [4] of the fluctuating properties of the flow under consideration.

The objective of this thesis is to use one of the classical techniques to detect acoustic waves in a normal impedance tube. These waves, unlike the flow fields in the previous studies, produce very small density gradients, and there is not a mean flow. If successful, this technique could be used to study various acoustic fields. One immediate application is the characterization of compliant back plate Helmholtz resonators [5] at the Interdisciplinary Microsystems Laboratory at the University of Florida using the normal impedance tube. These resonators will later serve as fundamental components of the electromechanical acoustic liner used for jet noise suppression. A quantitative optical flow visualization technique can be used to study phenomena (such as scattering effects in the acoustic field) that cannot otherwise be determined quantitatively using only microphone measurements.

1.1 Basic Schlieren Method

Of all the flow-visualization techniques mentioned earlier, shadowgraph is perhaps the simplest. Shadowgraphy is often used when the density gradients are large. This technique can accommodate large subjects and is relatively simple in terms of materials

required. The primary component consists of a point light source. The resulting shadow effect produced by the refractive-index field can be observed on an imaging surface. In terms of cost, this method is probably the least expensive technique to set up and operate. However, this system is not very sensitive. Also it is not a method suitable for quantitative measurements of the fluid density. However, it is a convenient method for obtaining a quick survey of flow fields with varying density, particularly shock waves. Another commonly used flow visualization technique is the interferometric technique [1]. It is highly sensitive and can provide quantitative information. However, such systems are expensive, complex to set up, and can only deal with relatively small subjects.

A shadowgraph system can be converted into a schlieren system with a slight modification in its optical arrangement. Schlieren systems are intermediate in terms of sensitivity, system complexity, and cost. The German word "schliere" means "streaks," since the variation in the refractive index show up as streaks. It was used in Germany for detection of an inhomogeneous medium in optical glass, which is often manifested in the form of streaks. In principle, the light passing through a medium with relatively small refractive differences bends light to directions other than the direction of propagation of light.

The simple schlieren set-up consists of optics to produce a point-light source, two lenses, a knife-edge and a screen. The point light source is placed at the focus of Lens 1.

The lens produces parallel light beams, which pass through the test section and are made convergent by the second lens called the schlieren head (Lens 2). An image of the light source is formed at the focal point of the schlieren head.

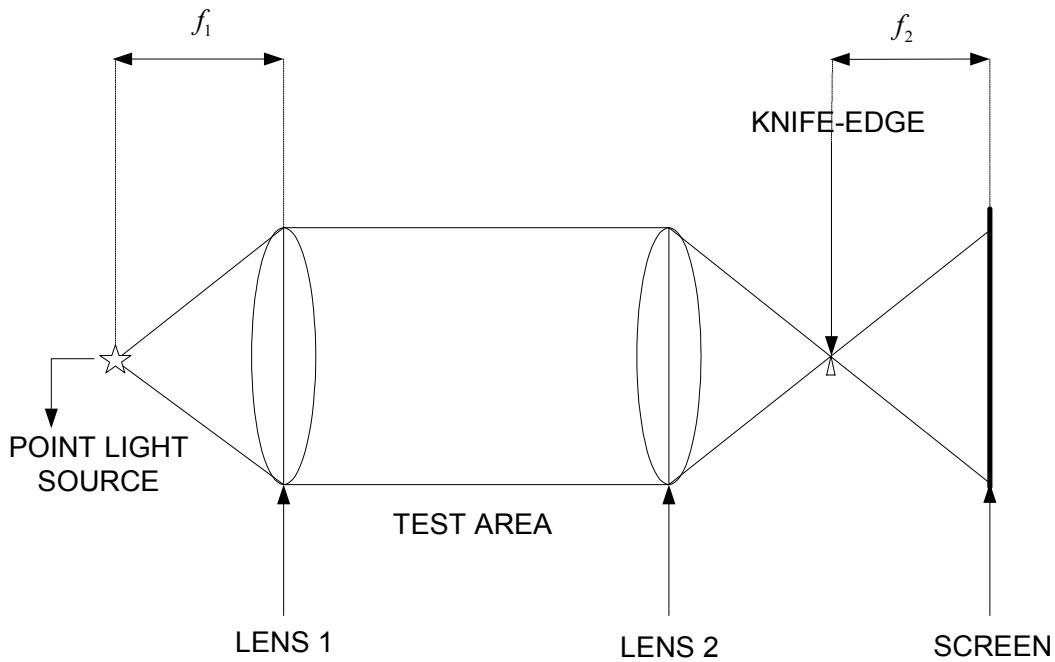

Figure 1-1: Simple schlieren setup.

At this position, a knife-edge (oriented perpendicular to the desired density gradient component) cuts off a certain portion of the light-source image and reduces the intensity of the recorded image plane. The edge is adjusted so that, if an optical disturbance is introduced such that a portion of the image of the source is displaced, the illumination of the corresponding part of the image on the screen will decrease or increase according to whether the deflection is toward or away from the opaque side of the knife edge. Building on this model an extended light source is considered in Chapter 2. Schlieren systems can be configured to suit many different applications and sensitivity requirements. They can be used for observing sound waves, shock waves, and flaws in glass. Its principal limitations are field size (limited by the diameter of the optical components) and optical aberrations.

1.2 Optical Deflectometer

Optical deflectometry involves the direct measurements of the density gradient in a flow using the schlieren technique. The conventional schlieren methods measure the total angular deflection experienced by a light ray while crossing the working section. This deflection can be directly related to the illumination of the image on the screen.

The quantitative version of the schlieren technique involves the determination of the density gradient component from the measured deflection. Experimental calibration and theory is used to characterize the relationship between light intensity fluctuation and density gradient. An adaptor is flush mounted onto the screen, which is connected to a photo-sensor module using a fiber optic cable. The photosensor detects the instantaneous fluctuations in light intensity in the schlieren image and converts the optical signal to an electrical signal.

1.3 Review of an Optical Deflectometer

The first important contribution to the development of the deflectometer was made by Foucault [4] by using an explicit cutoff in the form of a knife edge for the schlieren measurements. At the same time, the measurement technique was re-invented by Toepler [4] who named it "schlieren." Though the knife edge was not developed by Toepler, he has been given credit historically for developing the schlieren imaging technique.

The method was recognized to be a very valuable tool and used by many eminent scientists (Wood, Prandtl, etc.) [4]. Principles and experimental setup of schlieren techniques [3] were later explained by Holder and North in 1963 as part of the Notes on Applied Science and was published by the National Physical Laboratory. Fisher and Krause measured the light scattered [6] from two optical beams crossed in the region of

interest in a turbulent air jet. By cross-correlating the signal from each beam, information on the behavior of scatterer number-density near the intersection point was determined.

It was observed that this method was sufficiently general and independent of the method employed to obtain the desired fluctuation of light intensity. Taking advantage of this fact, Wilson and Damkevala [7] adapted a cross-correlation technique to obtain statistical properties of scalar density fluctuation. In their method, two schlieren systems are used, each of which gives signals in the flow direction integrated along the beam path. The optical beams are made to intersect in the turbulent field and, with the further assumption of locally isotropic conditions, the cross-correlation of the two signals and the local mean–square density fluctuation in the beam intersection point are determined.

Davis [8] used a single-beam schlieren system and made a series of measurements to investigate the density fluctuations present in the initial region of a supersonic axi-symmetric turbulent jet. The difference in distribution of density fluctuation due to preheating was observed using this method. Later, a quantitative schlieren technique was used by Davis [9] to determine the local scales and intensity of turbulent density fluctuations.

Recently, McIntyre et al. [4] developed a technique called “optical deflectometry” that was well suited to the study of coherent structures in compressible turbulent shear flows. A fiber-optic sensor was embedded in a schlieren image to determine the convective velocities of large-scale structures in a supersonic jet shear layer. The relative simplicity, low cost, and excellent frequency response of the optical deflectometer makes it an ideal instrument for turbulence measurements, especially in high-Reynolds number

flows. But one of its drawbacks is that it provides the information integrated along the beam path. This limitation can be removed using a sharp focusing schlieren [4].

Weinstein [10] has recently provided the analysis and performance of a high-brightness large-field focusing schlieren system. The system was used to examine complex two- and three-dimensional flows. Diffuse screen holography was used for three-dimensional photography, multiple colors were used in a time multiplexing technique, and focusing schlieren was obtained through distorting optical elements.

Also, Weinstein [11] described techniques that allow the focusing schlieren system to be used through slightly distorting optical elements. It was also mentioned that the system could be used to examine complex two- and three-dimensional flows.

Alvi and Settles [12] refined the quantitative schlieren system combining the focusing schlieren system with an optical deflectometer. This instrument is capable of making turbulence measurements and was verified by measurements of Kelvin-Helmholtz instabilities produced in a low-speed axisymmetric mixing layer.

Garg and Settles [13] used the technique for the measurements of density gradient fluctuations confined to a thin slice of the flow field. The optical deflectometer was used to investigate the structure of a two-dimensional, adiabatic, boundary layer at a free stream Mach number of 3. The results obtained were found to be in good agreement with that obtained using a hot wire anemometer. This result helped validate the new measurement technique. Further, Garg et al. [14,15] used the light-intensity fluctuations in a real-time schlieren image to obtain the quantitative flow-field data in a two-dimensional shear layer spanning an open cavity. Instantaneous density gradient and density fields were obtained from the data collected. With the help of a reference

microphone, phase- locked movies were created. Surveys were carried out for a Mach 0.25 cavity shear layer using the schlieren instrument as well as hot-wire anemometer. The results showed that the growth rates of instability waves in the initial "linear" region of the shear layer could accurately be measured using this technique.

A similar procedure was adopted by Kegerise et al. [16] using the optical deflectometer with various higher-order corrections to experimentally study the modal components of the oscillations in a cavity flow field. Shear layer and acoustic near field measurements were performed at free stream Mach numbers of 0.4 and 0.6. Standing wave patterns were identified in the cavity using this method. These experiments have considerably improved the understanding of the cavity physics that cause and maintain self-sustaining oscillations.

In the most recent development, Cattafesta et al. [17] verified using primary instantaneous schlieren images that the multiple peaks of comparable strength in unsteady pressure spectra, which characterize compressible flow-induced cavity oscillations, are the results of mode-switching phenomenon.

1.4 Research Objectives

The objective of the current project is to develop a system, which can measure the density gradient in a normal impedance tube. This represents an intermediate step towards a focused schlieren system for normal acoustic impedance tube measurements for applications described earlier in the chapter. It can be seen that all the measurement techniques used till date like the microphone method are flow intrusive. The main advantage of this technique is that there is no flow intrusion. Also two dimensional flow fields and effects of scattering can be determined using this technique. The aim of the

experiment ultimately is to verify the results obtained from the deflectometer using the microphone measurements, thereby developing a more efficient technique.

1.5 Thesis Outline

The thesis is organized into six chapters. This chapter presents the introduction, background, and application of the optical deflectometer. Chapter 2 presents the theory of the schlieren system as well as that of the normal impedance tube. Theoretical formulations for the sensitivity are also developed in this chapter. Chapter 3 discusses the steps involved in setting up the system and the plane wave tube including the data acquisition system. Chapter 4 presents the data analysis using the cross spectral technique. It also describes the static and dynamic calibration of the system. Chapter 5 presents the numerical and experimental results obtained during the course of this project. Chapter 6 presents concluding remarks, proposed design modifications, and future work for the optical deflectometer.

CHAPTER 2
OPTICAL DEFLECTOMETER

As discussed in Chapter 1, the goal of this project is to design and test an optical system capable of measuring the density gradient of plane waves in an impedance tube. Therefore, this chapter discusses the theory behind an optical deflectometer and the sensitivity of the system. First, an expression for the pressure fluctuation in a normal impedance tube for plane waves is derived. The pressure fluctuation is then related to the density and density gradient, which causes the refraction of the light rays. Second, the relationship between the light intensity fluctuation and the density gradient in the flow-field is presented. The sensitivity of the system with regard to the various optical parameters is then derived.

2.1 Normal Impedance Tube

The flow visualized by the deflectometer is generated in a rectangular normal impedance tube. In the next section, theoretical derivations of the acoustic field within the tube are given for plane wave.

Single Impedance Termination. The acoustic flow field is thus comprised of waves that have uniform pressure in all planes perpendicular to the direction of propagation and are termed as plane waves. The plane wave assumption is valid below the cut-on frequency [18] of a square tube, given by $\frac{c_\infty}{2s}$, where c_∞ is the isentropic sound speed and s is the width of the normal impedance tube. As can be seen in Figure

2-1, an acoustic driver ultimately generates plane waves on one end of the impedance tube of length l and the specimen is placed

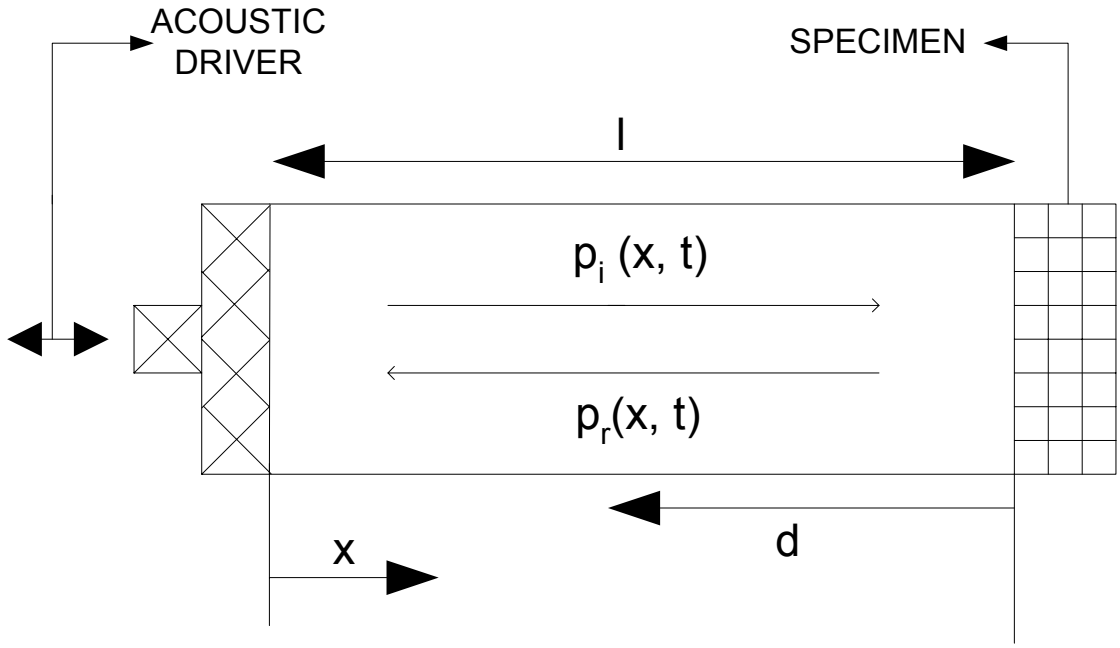

Figure 2-1: Plane wave tube.

at the other end. The pressure p inside the tube at a position d is given by

$$p(d) = p_i \, \mathrm{e}^{ikd} + p_r \, \mathrm{e}^{-ikd}, \tag{2-1}$$

where p_i and p_r are the incident and reflected pressure respectively. Here $p_i = A\,\mathrm{e}^{-ikl}$ and $p_r = B\,\mathrm{e}^{ikl}$ are phasors. The time-harmonic dependence, $e^{i\omega t}$, is implicit in p. The complex reflection coefficient R is defined as

$$R = \frac{p_r}{p_i}. \tag{2-2}$$

Substituting Equation 2-2 in Equation 2-1, the expression for $p(d)$ becomes

$$p(d) = p_i(\mathrm{e}^{ikd} + R\,\mathrm{e}^{-ikd}). \tag{2-3}$$

In a plane wave, the velocity can be related to pressure through the equation $u = \frac{p}{\rho c}$, and, the velocity in the plane wave tube can be written as

$$u(d) = \frac{p_i}{\rho c_\infty}(\mathrm{e}^{ikd} - \mathrm{R} \cdot \mathrm{e}^{-ikd}). \tag{2-4}$$

The specific acoustic impedance is defined as the ratio of the pressure to the velocity in the tube

$$Z(d) = \frac{p}{u} = \rho c_\infty \frac{(\mathrm{e}^{ikd} + R \cdot \mathrm{e}^{-ikd})}{(\mathrm{e}^{ikd} - R \cdot \mathrm{e}^{-ikd})}. \tag{2-5}$$

When $d = 0$, the impedance must equal the terminating impedance, which is the impedance of the specimen

$$Z_n = \rho c_\infty \frac{(1+R)}{(1-R)}. \tag{2-6}$$

Solving for R gives

$$R = \frac{Z_n - \rho c_\infty}{Z_n + \rho c_\infty}. \tag{2-7}$$

When R is not equal to zero a standing wave pattern results and is often characterized by the [18] pressure standing wave ratio (SWR)

$$SWR = \frac{|p_{\max}|}{|p_{\min}|} = \frac{1+|R|}{1-|R|}, \tag{2-8}$$

which is the ratio of maximum to minimum pressure in the tube. The complex reflection factor R can be represented in polar notation as

$$R = |R| e^{j\phi_r}. \tag{2-8}$$

The reflection factor R can also be split into real and imaginary components as

$$R = R_{real} + jR_{img} \tag{2-9}$$

where $R_{img} = |R| \sin \phi_r$ and $R_{real} = |R| \cos \phi_r$

The reflection coefficient R can be measured [19] [20] using the two-microphone method.

$$R = |R| e^{i\phi_R} = \frac{H - e^{-iks}}{e^{jks} - H} e^{j2k(l' + s)}. \tag{2-10}$$

where s is the center-to-center spacing between the two microphones, l' is the distance from the test sample to the nearest microphone and H is the geometric mean of the measured transfer function between the microphones

$$H = \sqrt{H_1 H_2}, \tag{2-11}$$

and H_1 and H_2 are the transfer functions for the microphones in the standard and switched configurations.

The normalized impedance can be obtained by substituting Equations 2-9 in Equation 2-7 as

$$Z_{real} = \frac{1 - R_{real}{}^2 - R_{img}{}^2}{(1 - R_{real})^2 + R_{img}{}^2} \tag{2-12}$$

and

$$Z_{img} = \frac{2R_{img}}{(1 - R_{real})^2 + R_{img}{}^2} \tag{2-13}$$

2.2 Theory of a Schlieren System

This section summarizes the theory of operation of a simple [3] schlieren system. Details of the quantitative part of the experimental set-up are discussed in Chapter 4.

2.2.1 Deflection of Light by a Density Gradient

In the experiments being conducted the refractive index of the test section varies along the direction of propagation. This is caused by the variation in the density of the medium. For an isentropic process, pressure and density fluctuations are related by

$$p = \rho c_{\infty}^{2}. \tag{2-13}$$

The pressure gradient in the x-direction is

$$\frac{\partial p}{\partial x} = c^{2}\frac{\partial \rho}{\partial x}. \tag{2-14}$$

From the above equation, it can be seen how the density varies in the x direction in an impedance tube. Substituting Equation 2-3 in Equation 2-14 and taking the derivative w.r.t d, we obtain the density gradient as

$$\frac{\partial \rho}{\partial d} = \frac{p_i jk(e^{jkd} - Re^{-jkd})}{c^{2}}. \tag{2-15}$$

The aim of the experimental program is to determine this density gradient using the schlieren system.

In the case of gaseous substances the refractive index, n is related to density by the Gladstone-Dale equation [3] (Equation 2-16).

$$n - 1 = k\rho. \tag{2-16}$$

where $k = 2.259 \times 10^{-4}\ m^{3}/kg$ is the Gladstone-Dale constant. If there exists a gradient of refractive index normal to the light rays in a working section, the rays will be deflected since light travels more slowly in a non-vacuum media, with the velocity given by

$$c = c^{*}/n, \tag{2-17}$$

where c^* is the velocity of light in vacuum. The basis of the schlieren technique relies on the fact that the deflection of the light rays is a measure of the first derivative of the density with respect to distance (i.e., the density gradient). The derivation [1] is as follows:

The curvature of the ray is proportional to the refractive-index gradient in the direction normal to the ray. If we take the z - axis as the direction of the undisturbed ray, the curvatures in the $x-y$ and $y-z$ planes respectively are given by (see Appendix B)

$$\frac{\partial^2 x}{\partial^2 z} = \frac{1}{n}\frac{\partial n}{\partial x}, \tag{2.18}$$

$$\frac{\partial^2 y}{\partial z^2} = \frac{1}{n}\frac{\partial n}{\partial y}. \tag{2.19}$$

The total angular deflection in the $x-z$ and $y-z$ planes are taken as ε'_x and ε'_y respectively

$$\varepsilon'_x = \int \frac{1}{n}\frac{\partial n}{\partial x} dz \tag{2-20}$$

$$\varepsilon'_y = \int \frac{1}{n}\frac{\partial n}{\partial y} dz \tag{2-21}$$

If the optical disturbance is in the working section of a wind tunnel, the light ray will be refracted on leaving the tunnel so that

$$n \sin \varepsilon' = n_0 \sin \varepsilon, \tag{2-22}$$

where n_o is the refractive index of the air surrounding the tunnel, and n is the refractive index in the working section. Thus, assuming small angular deflections, the final angular deflections ε measured beyond the tunnel are

$$\varepsilon_x = \frac{1}{n_0}\int \frac{\partial n}{\partial x} dz, \tag{2-23}$$

$$\varepsilon_y = \frac{1}{n_0}\int \frac{\partial n}{\partial y} dz. \tag{2-24}$$

Since the refractive index of air is approximately equal to 1, the expressions can be written as

$$\varepsilon_x = \int \frac{\partial n}{\partial x} dz. \tag{2-25}$$

$$\varepsilon_y = \int \frac{\partial n}{\partial y} dz. \tag{2-26}$$

In the case of two-dimensional flow in a tunnel of width W, the expressions become

$$\varepsilon_x = W\frac{\partial n}{\partial x}, \tag{2-27}$$

$$\varepsilon_y = W\frac{\partial n}{\partial y}. \tag{2-28}$$

where the deflection is toward the region of highest density.

2.2.2 The Toepler Method

In the Toepler schlieren system [4] a rectangular slit source is used, with the long dimension of the slit parallel to the knife-edge. As shown in Figure 2-2 an image of the slit source produced at the knife-edge, of which only a part of height a is allowed to pass over the knife-edge. With a homogeneous test field, the recording plane is evenly illuminated with an intensity $I(x, y)$= const, which is proportional to the value of a. Light rays deflected by an angle ε_x due to a disturbance in the test field cause a (vertical) shift of the light source image by an amount Δa

$$\Delta a = f_2 \tan \varepsilon_x .$$

For small values of deflection since $\tan(\varepsilon_x)$ is approximately ε_x, so

$$\Delta a = f_2 \varepsilon_x , \tag{2-29}$$

where f_2 is the focal length of Lens 2.

Let P be the power of the light beam. The power can be defined as $P = IA$ where I is the intensity (Power per unit area) and A is the illumination area. Assuming the power to be conserved between the knife-edge and the screen

$$I_{KE} A'_{KE} = I_{screen} A_{screen} \tag{2-30}$$

or

$$I_{screen} = \frac{I_{KE} A'_{KE}}{A_{screen}} \tag{2-31}$$

where I_{KE} is the intensity of light passing the knife-edge. In the case of half knife-edge cut-off, the image on the rear side of the knife-edge has a height b and breadth $\frac{a}{2}$ and hence the area

$$A_{KE}' = b\frac{a}{2}. \tag{2-32}$$

Equation 2-31 can be expressed as

$$I_{screen} = \frac{I_{KE} ab}{2A_{screen}} \tag{2-33}$$

When the light source image shifts by an amount Δa

$$I_{screen} + \Delta I = \frac{I_{KE}\left(\frac{a}{2} + \Delta a\right)b}{A_{screen}} \tag{2-34}$$

And the intensity change on the screen can be expressed as

$$\Delta I = \frac{I_{KE}\Delta ab}{A_{screen}} \tag{2-35}$$

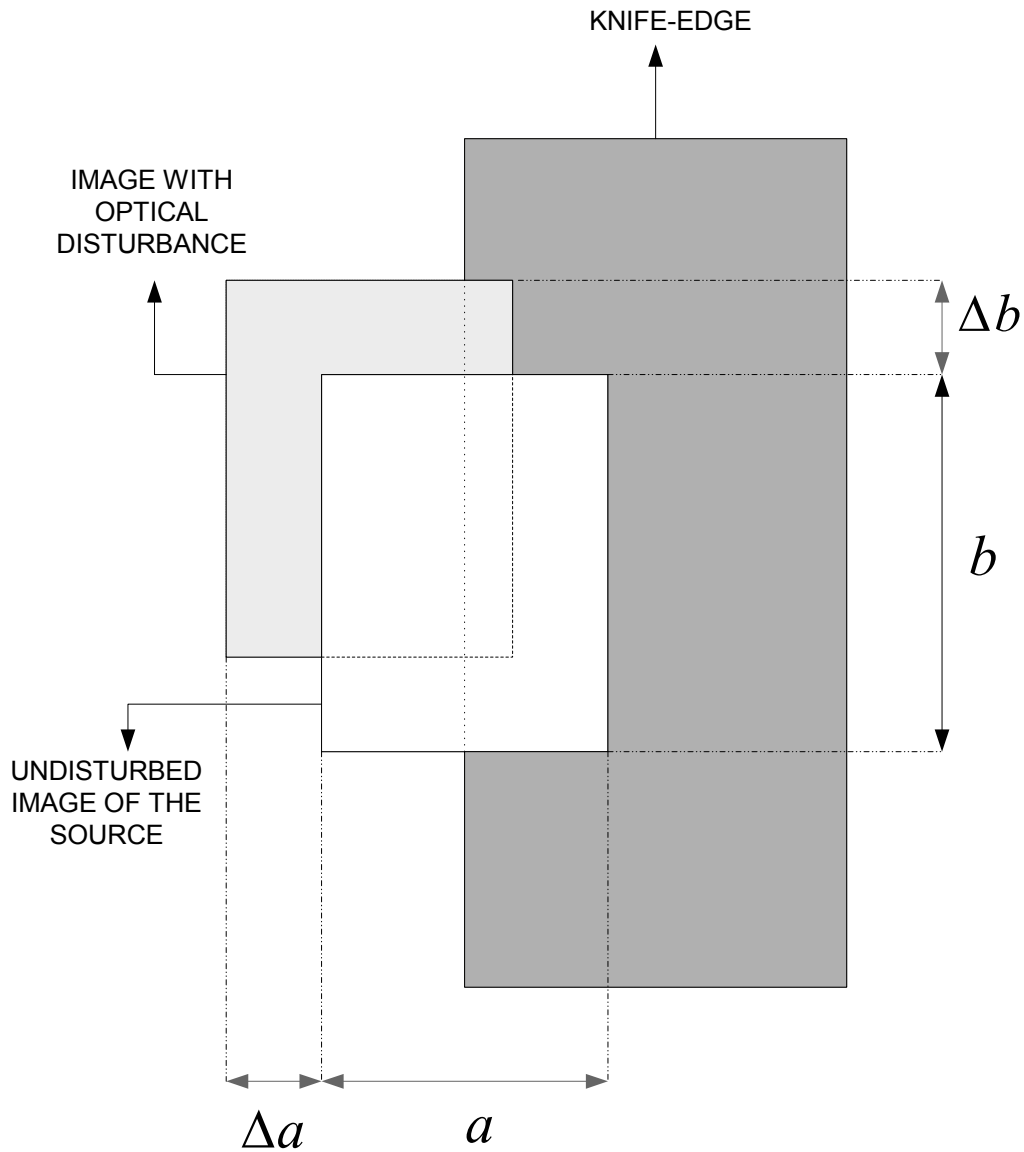

Figure 2-2**:** Light source in the plane of the knife-edge

The recording plane receives an intensity changed by ΔI in the corresponding image point; the relative intensity change also known as contrast C is obtained from Equation 2-33 and Equation 2-35 as

$$C \equiv \frac{\Delta I}{I_{screen}} = \frac{2\Delta a}{a} = \frac{2f_2}{a}\varepsilon_x. \tag{2-36}$$

The contrast sensitivity is given by

$$S_c \equiv \frac{dC}{d\varepsilon} = \frac{2f_2}{a} \tag{2-37}$$

This sensitivity [14] in terms of the contrast is important in the traditional qualitative method since the photographic films are sensitive relative intensity changes.

But in the case of quantitative schlieren technique, the photo-sensor can detect absolute light intensity change. Hence the quantitative sensitivity is defined as

$$S_q \equiv \frac{d(\Delta I)}{d\varepsilon} = \frac{2f_2}{a} I_{screen} \tag{2-38}$$

Substituting the expression for I_{screen} we obtain

$$S_q \equiv \frac{d(\Delta I)}{d\varepsilon} = \frac{f_2 I_{KE} b}{A_{screen}} \tag{2-39}$$

Using the value of angular deflection from Equation 2-27 we obtain

$$\frac{\Delta I}{I_{screen}} = \frac{2f_2 W}{a}\frac{\partial n}{\partial x} \tag{2-40}$$

Using the Gladstone-Dale Equation 2-16 we get

$$\frac{\Delta I}{I_{screen}} = \frac{2kf_2 W}{a}\frac{\partial \rho}{\partial x}. \tag{2-41}$$

Alternatively, the relative intensity change in the *y* direction can be obtained by turning the knife-edge by 90^{o,} and the relative intensity change is

$$\frac{\Delta I}{I_{screen}} = \frac{2kf_2 W}{a}\frac{\partial \rho}{\partial y}. \tag{2-42}$$

The schlieren system “sensitivity” is often equated to the relative change in illumination intensity, which is a measure of the refractive index or density gradient in the direction normal to the knife-edge.

In the case of a normal impedance tube with plane waves, since the density gradient exists only in the x direction, the measured intensity change is therefore given by Equation 2-41.

2.3 Sensitivity Analysis

A detailed sensitivity analysis of the optical system is performed in this section. Since a point source, discussed in Chapter 1, is not realistic, an extended light source is considered in the following derivation. The extended light source is in the form of a rectangular aperture, and a condenser lens is used to focus the light beams from the source at the rectangural aperture. The experimental set-up will be discussed in detail in Chapter 3.

Figure 2-3 shows the ray diagram of the schlieren setup. It can be seen that the light beams from the source are focused by the condenser lens at the rectangular aperture. From this point onwards, the rectangular aperture/slit with height h and width d is treated as the source. Lens 1 is placed at a distance equivalent to its focal length from the slit and collimates the light beam. Since the light source is no-longer a point source, Lens 1 no longer produces rays parallel to the optical axis. It can be taken [4] as an array of the source distributed along the height h. This can be proved by taking four rays from the top of the slit into consideration. Ray (1) passes through the center of the lens and is undeviated. Ray (2) which initially travels parallel to the optical axis is deviated so that it passes through the focal point. It can be seen from the figure that these two rays comes out of the lens parallel to each other. Also any ray originating from the top of the slit emerges out of the lens parallel to Ray (1) and Ray (2). Two such rays, Ray (3) and Ray (4) are then taken into consideration. Ray (3) passes through the focal point of

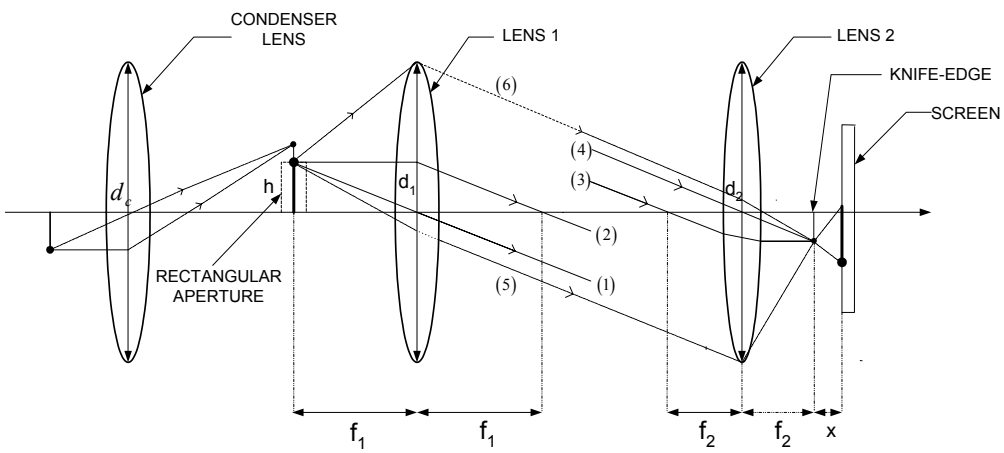

Figure 2-3: Ray diagram of the schlieren setup.

Lens 2 and is deviated to travel parallel to the optical axis. Ray (4) passes through the center of the lens and is undeviated. These two beams are focused at the focal point of Lens 2, where the knife-edge is placed. The image is further magnified and viewed on the screen placed at a distance x from the knife-edge. Rays (5) and (6) are the extreme rays originating from the top of the slit.

The power of the light beam emitted by the slit is

$$P_{slit} = I_{slit} A_{slit} = I_{slit}(dh). \tag{2-43}$$

It is assumed that the power is conserved through out the optical setup for a case without the knife-edge, therefore $P = IA$ is constant.

$$I_{slit} A_{slit} = I_{screen/wo} A_{screen},$$

or

$$I_{screen/wo} = \frac{I_{slit} dh}{A_{screen}}. \tag{2-44}$$

where $I_{screen/wo}$ is the intensity of the image on the screen with out knife-edge.

Also, as the light passes through any lens, both source dimensions are magnified such that the image area at any point will be $(md)(mh)$ or $m^2 dh$ where m is the magnification ratio defined as the ratio of image dimension to object dimension. For a

lens combination, as in Figure 2-3, the total magnification is the product of each lens magnification such that

$$m_{screen} = m_1 m_2 m_3$$

And, area of the image on the screen is

$$A_{screen} = \left(m_{screen}\right)^2 dh, \tag{2-45}$$

where m_{screen} is the magnification on the screen.

In the case of a bi convex lens, the magnification is also equal to the ratio of the image distance from the lens to the object distance from the lens. Therefore the magnification due to the Lens 1 is

$$m_1 = \frac{\infty}{f_1}, \tag{2-46}$$

since the slit is placed at the foal point of Lens 1 and the image is formed at infinity.

The magnification due to the Lens 2 is

$$m_2 = \frac{f_2}{\infty}, \tag{2-47}$$

since parallel rays falls on the lens, and the image is formed at the focal point of Lens 2.

The magnification between the focal point of Lens 2 and the screen (see Appendix A) using similar triangles is

$$m_3 = \frac{\frac{d_2}{2} - \frac{f_2}{f_1} h}{\frac{f_2^{\,2}}{f_1} h} x + 1 \tag{2-48}$$

where x is the distance between the knife-edge and the traverse. Hence the total transverse magnification on the screen is

$$m_{screen} = \left[\frac{\infty}{f_1}\right]\left[\frac{f_2}{\infty}\right]\left[\frac{\frac{d_2}{2} - \frac{f_2}{f_1}h}{\frac{f_2^2}{f_1}h}x + 1\right],$$

$$m_{screen} = \left[\frac{f_2}{f_1}\right]\left[\frac{\frac{d_2}{2} - \frac{f_2}{f_1}h}{\frac{f_2^2}{f_1}h}x + 1\right], \tag{2-49}$$

Substituting Equation 2-49 into Equation 2-45 the area of the screen can be expressed as

$$A_{screen} = \left[\frac{f_2}{f_1}\right]^2\left[\frac{\frac{d_2}{2} - \frac{f_2}{f_1}h}{\frac{f_2^2}{f_1}h}x + 1\right]^2 dh. \tag{2-50}$$

The resulting intensity on the image plane is

$$I_{screen/wo} = \frac{I_{slit}}{\left[\frac{f_2}{f_1}\right]^2\left[\frac{\frac{d_2}{2} - \frac{f_2}{f_1}h}{\frac{f_2^2}{f_1}h}x + 1\right]^2} \tag{2-51}$$

In practice however, a knife-edge is placed at the focal point of Lens 2. There is no power loss prior to the knife-edge location. Hence

$$I_{KE}A_{KE} = I_{source}A_{source}, \tag{2-52}$$

where I_{KE} is the light intensity, and A_{KE} is the area illuminated on the front side of the knife-edge.

$$A_{KE} = \left(m_{KE}\right)^2 dh. \tag{2-53}$$

Also, the magnification at the knife-edge can be calculated as $m_{KE} = m_1 * m_2 = \frac{f_2}{f_1}$.

Substituting in Equation 2-52, the light intensity at the knife-edge can be expressed as

$$I_{KE} = \frac{I_{source}}{\left[\frac{f_2}{f_1}\right]^2}. \tag{2-54}$$

The knife-edge blocks a portion of the light as shown in Figure 2-2. In the case of half-cutoff, the area of the image on the rear side of the knife-edge A_{KE}' (where the prime superscript denotes a position after the knife-edge) has already been derived in Equation 2-32.

As in section 2.2.2, the power can be assumed to be conserved from the knife-edge to the screen and Equation 2-30 can be applied. Also, the constants A_{screen} and I_{KE} can be obtained from Equation 2-50 and Equation 2-54 respectively. The expression for the intensity of the image on the screen (Equation 2-33) can be modified as

$$I_{screen} = \frac{I_{source} ab}{2\left[\frac{f_2}{f_1}\right]^4 \left[\frac{\frac{d_2}{2} - \frac{f_2}{f_1}h}{\frac{f_2^2}{f_1}h} x + 1\right]^2 dh} \tag{2-55}$$

and the quantitative sensitivity (Equation 2-39) of the instrument in the x axis can be expressed as

$$S_q \equiv \frac{I_{source} f_2 b}{\left[\frac{f_2}{f_1}\right]^4 \left[\frac{\frac{d_2}{2} - \frac{f_2}{f_1}h}{\frac{f_2^2}{f_1}h} x + 1\right]^2 dh} \tag{2-56}$$

Since

$$b = (m_1 m_2)h = \frac{f_2}{f_1} h$$

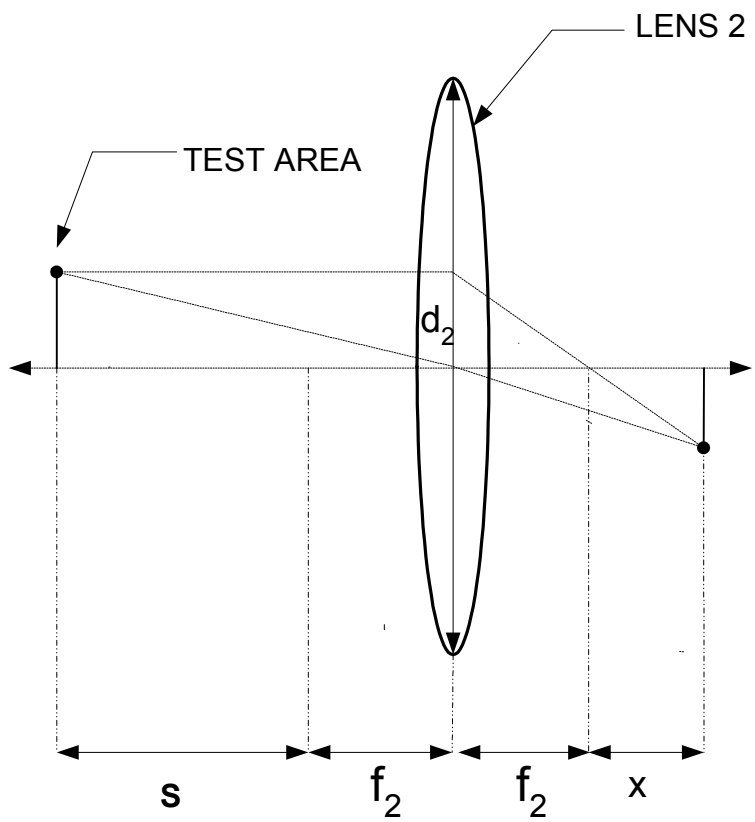

Figure 2-4: Schlieren head with the conjugate plane.

Equation 2-56 can be written as

$$S_q \equiv \frac{I_{source} f_2}{\left[\frac{f_2}{f_1}\right]^3 \left[\frac{\frac{d_2}{2} - \frac{f_2}{f_1} h}{\frac{f_2^2}{f_1} h} x + 1\right]^2 d} \tag{2-57}$$

If the test area is placed at a distance s from the focal point of Lens 2, the real image is formed at the conjugate plane. Using the thin lens formula, we obtain

$$x = \frac{f_2^2}{s} \tag{2-58}$$

Hence if the screen is placed at the conjugate plane the sensitivity can be expressed as

$$S_q \equiv \frac{I_{source} f_2}{\left[\frac{f_2}{f_1}\right]^3 \left[\frac{\frac{d_2}{2} - \frac{f_2}{f_1} h}{\frac{hs}{f_1}} + 1\right]^2 d} \tag{2-59}$$

The equation can be non-dimentionalized as

$$\frac{S_q}{I_{source}} \equiv \frac{f_2}{\left[\frac{f_2}{f_1}\right]^3 \left[\frac{\frac{d_2}{2} - \frac{f_2}{f_1} h}{\frac{hs}{f_1}} + 1\right]^2 d} \tag{2-60}$$

It can thus be seen that the quantitative sensitivity is a function of various optical parameters. Once the field of view d_2 and the conjugate plane distance x are fixed, an optimal value for $\frac{f_2}{f_1}$ (ratio of the focal length of Lens 2 and Lens 1) and $\frac{h}{d}$ (Ratio of the height and width of the slit), can be obtained for maximum sensitivity (taking diffraction effects into consideration).

CHAPTER 3
EXPERIMENTAL SET UP

Flow visualization and data acquisition using the optical deflectometer was performed at the Interdisciplinary Microsystems Laboratory at the University of Florida. This chapter discusses the experimental setup in detail. The chapter is divided into three sections. The first section describes the optical system used for detecting the density gradient field. The second section describes the normal impedance tube that generates the acoustic field. The last section deals with the data acquisition system used in detecting the light intensity fluctuations.

3.1 Basic Schlieren Setup

The schlieren setup used in the optical deflectometer is shown in figure 3-1. As discussed earlier, the point light source mentioned in Chapter 1 is not realistic. Hence an extended light source is created using a $2mm - 2mm$ rectangular aperture. A $100\ W$ tungsten- halogen lamp with a custom aluminum housing is used as the light source. A combination of compressed air and a fan is used to cool the housing. A DC power supply (Twinfly model $P1-100-12$) is used to supply $12\ V$ to the lamp. The light passes through an 8-inch long tube for minimal loss. A condenser lens (Oriel model 39235) of diameter $50.8\ mm$ and focal length $100\ mm$ is placed at the end of this tube. The lens is achromatic in nature and prevents chromatic aberrations. The beam that passes through the condenser lens is focused onto a rectangular aperture (Coherent model $61-1137$), which acts as the point source.

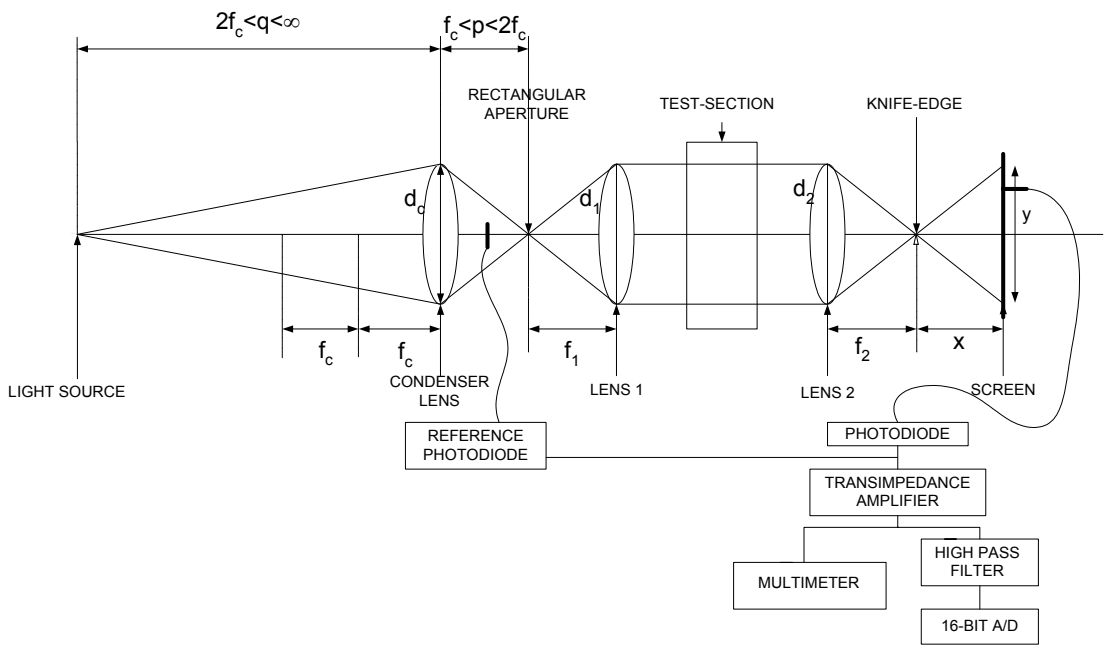

Figure 3-1**:** Deflectometer set-up.

The test-section is placed in between the two schlieren achromatic lens (Oriel model 39235) of diameter $50.8\ mm$ and focal length $100\ mm$, so that a collimated beam passes through the flow-field. The knife-edge consists of a razor blade and is placed on a $X-Y-Z$ positioning movement (Edmund Scientific Model $NT03-607$) for fine adjustments. The screen is made of translucent paper and is mounted on a traverse. All the optical components are mounted using mounting posts and holders. The system is placed on a rail (Edmund model $NT54-402$) so that the distance between various optical components can be adjusted easily.

3.2 Normal Impedance Tube

3.2.1 Components

The impedance tube shown in Figure 3-2 is straight and is of a constant square cross-section of width $25.4\ mm$ rigid, smooth, non-porous walls without holes or slits in

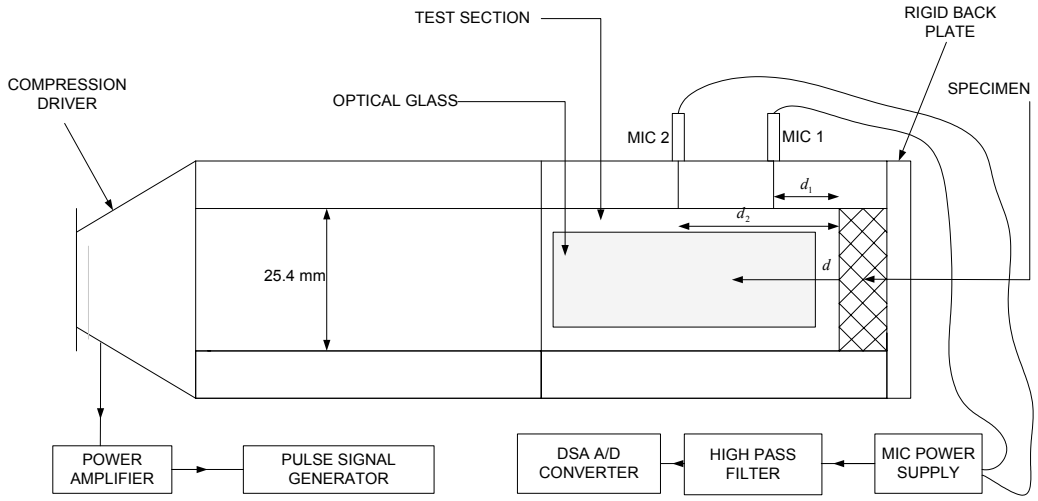

Figure 3-2: Normal impedance tube

the test section. The metal used for the construction of the plane-wave tube is aluminum It has a length of $0.724\ m$ with a cut-off frequency of $6.7\ kHz$ for the plane wave mode. The walls are $22\ mm$ thick so that incident sound produces no appreciable vibration and validates the rigid wall approximation. The test-section is placed on one end of the tube. A membrane loudspeaker/compression driver (JBL model $2426H$) is placed at the termination of the impedance tube at the end opposite to the sample holder. The loudspeaker is contained in a sound-insulating box in order to minimize the sound produced by the speaker. Sinusoidal oscillations are generated using a signal generator, which is the PULSE (B&K Type 2827-002) system in our case.

3.2.2 Fabrication of the Test Section

The test section was fabricated such that it can be attached to one end of the impedance tube. The transition from impedance tube to the test section is smooth and care is taken to minimize leakage at the joints. Optical glass is inserted at the front and rear side of the test section for visualizing the flow. The length of the window is

$0.17\ m$ and height $50.8\ mm$. The sample holder is fixed at the termination of the test-section. It is a

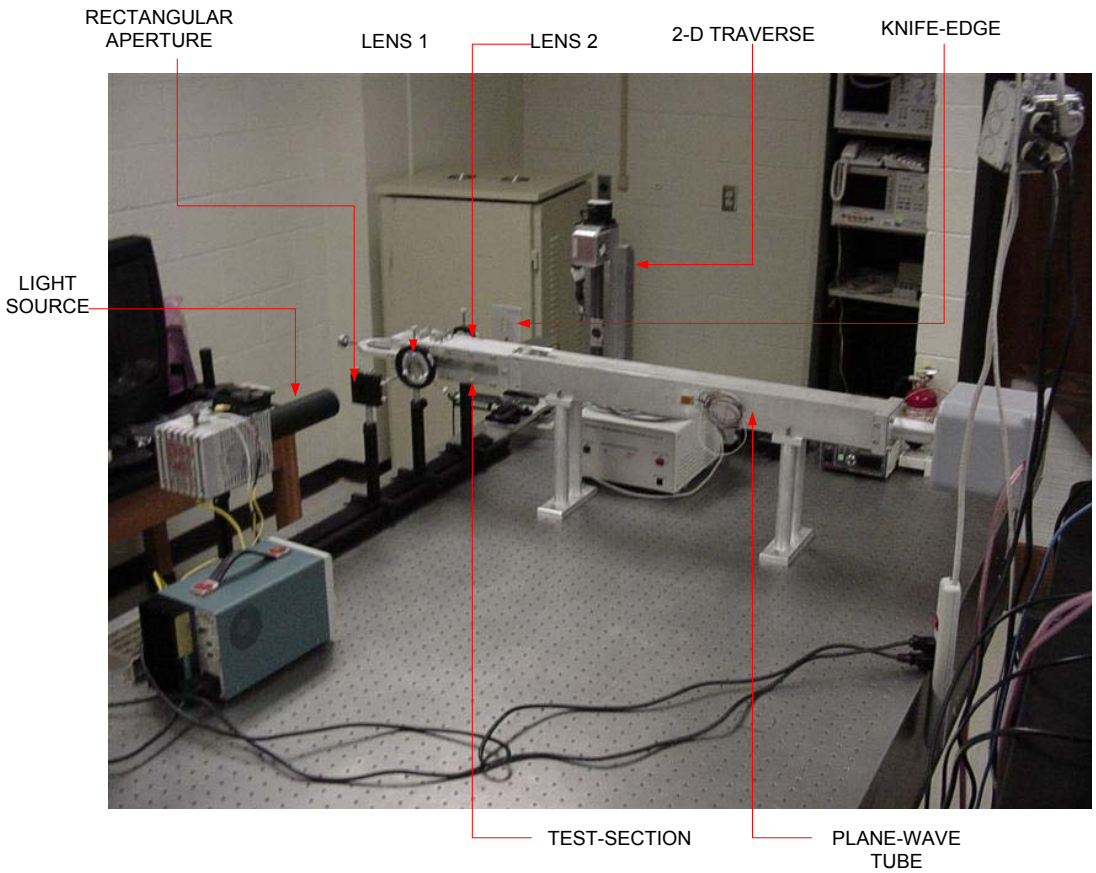

Figure 3-3: Setup for normal impedance tube.

separate unit and it is large enough to install test objects leaving air spaces of a required depth behind them. Since experiments were being conducted for a reflection coefficient of unity, the specimen used was made of aluminium and $22\ mm$ thick in order to provide sound hard boundary condition.

3.3 Data Acquisition System

The microphone signal and both the mean and the fluctuating signal of the photo detector were measured. The following equipment was used.

3.3.1 Photosensor Module

Data was acquired using two photodiode modules (Hamamatsu Model $H5784-20$). One detector was used to detect a reference signal (explained in Chapter 4) and the other measured the fluctuating light intensity on the screen. The sensitivity of the module is $255\times10^{6}\ V/lm$ and the output of the detector varies from -15 to $+15\ V$. The output-offset voltage was $-8.0\ mV$ and the control voltage of the photo-detector module was set at $0.35\ V$. The light is passed on to the photodiode through a fiber optic cable, which terminates in a SMA adaptor (Newport model $FP3-SMA$).

3.3.2 Positioning System

The screen with the photodiode is placed on a two-dimensional traverse (Velmex Model MB4012P40J-S4). The resolution of the traverse is $1.6\ \mu m$ and is controlled using a controller (Velmex Model VXM 1). The positioning system and data acquisition system was computer controlled using LabVIEW. For calibration of the system, the knife-edge was placed on a one-dimensional traverse (Newport model $ESP100$), which has a resolution of $1\ \mu m$.

3.3.3 Signal-Processing Equipment

The output signal of the photo-diode and the microphone are filtered using a computer optimized filter (Kemo Model $VBF35$ Multi-Channel Filter/Amplifier System) with a flat pass band and linear passband phase, that operates as a high pass filter with a cut-in frequency of $850\ Hz$. The filtered signal passes to a 16-bit A-D converter (National Instrument Model $NI4552$) to remove the low frequency components. The time invariant component of the signal is simultaneously sampled using a multimeter (Keithley model 2400). The entire process is computer controlled using LabVIEW.

CHAPTER 4
DATA ANALYSIS

This chapter discusses the quantitative extension of the schlieren technique, namely optical deflectometry. As discussed in Chapter 1, this involves the measurement of light-intensity fluctuations at a point on the image plane using a fiber optic sensor. The first part of this chapter deals with the static calibration, which relates light intensity fluctuations to the knife-edge deflection. Subsequently, the cross-spectral correlation technique used to determine the magnitude and phase of the density gradient relative to a reference microphone is described. In the last part of the chapter, dynamic calibration of the instrument using a laser impulse is discussed.

4.1 Calibration of the Optical Deflectometer

The objective of the calibration is to establish a relationship between the light intensity fluctuation and the density gradient. We take advantage of both theoretical and experimental methods to determine this relationship.

The relationship between the angular deflection and the variation in refractive index has already been derived in Chapter 2 in Equation 2-27 and Equation 2-28. Using the Gladstone-Dale relationship in Equation 2-16, assuming two-dimensional flow field, and $n_0 \approx 1$ for the surrounding air gives

$$\varepsilon_x \approx kW \frac{\partial \rho}{\partial x}. \tag{4-1}$$

Prior to the experiments, theoretical calculations were done in order to obtain an estimate of the range of the light intensity fluctuation due to the flow. The maximum

density gradient in the plane wave tube for a typical value of sound pressure level was compared to the maximum density gradient that can be detected by the system. This provides an estimate of the fraction of the linear operating range that is occupied by the light-intensity fluctuations.

It has already been derived (Equation 2-30) that the light intensity fluctuation is related to the angular deflection of the light rays. The image of the source at the knife-edge has been shown in Figure 2-2, and the parameters are described in Chapter 2. For a knife-edge at half cutoff,

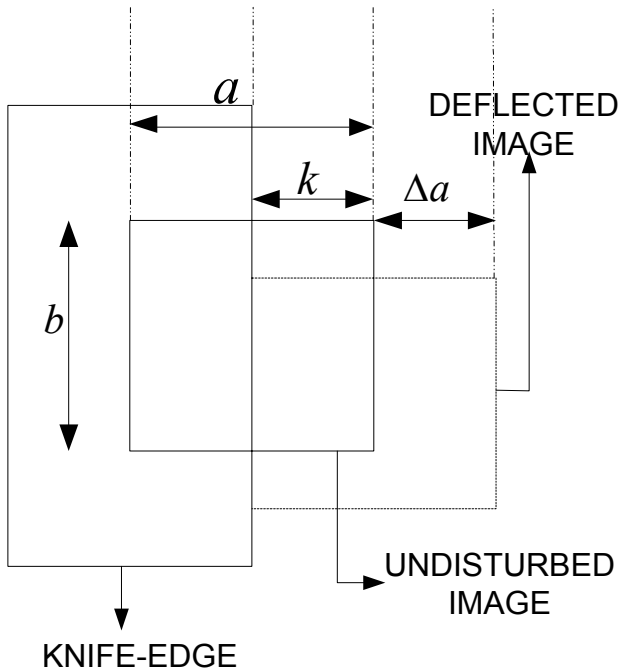

Figure 4-1: Light source in the plane of the knife-edge.

$$k = \frac{a}{2} \tag{4-2}$$

The maximum deflection in the light ray, which can be detected by the system, occurs at

$$\Delta a = \frac{a}{2} \tag{4-3}$$

This case has been shown in Figure 4-1. Substituting Equation 4-3 in Equation 2-29, $\Delta a = f_2 \varepsilon_x$, gives

$$\varepsilon_x = \frac{a}{2 f_2}. \tag{4-4}$$

To determine the maximum density gradient that can be detected by the system, combining Equation 4-4 and Equation 4-1 gives

$$\left.\frac{\partial \rho}{\partial x}\right)_{\max} = \frac{a}{2 f_2 k W}. \tag{4-5}$$

Also, the magnification of the source at the knife-edge is

$$m_{KE} = \frac{f_2}{f_1} \tag{4-6}$$

and

$$a = m_{KE} d, \tag{4-7}$$

where d is the width of the rectangular aperture. Using Equation 4-7, the density gradient can be rewritten as

$$\left.\frac{\partial \rho}{\partial x}\right)_{\max} = \frac{d}{2 f_1 k W}. \tag{4-8}$$

Substituting the value of the focal length $f_1 = 100\ mm$, the width of the test-section $W = 0.0254\ m$, and the value of $d = 2\ mm$, the maximum density gradient that can be detected by the schlieren system is $1.74 \times 10^3\ kg/m^3$.

The expression for the density gradient in the normal impedance tube is given by Equation 2-15. Differentiating with respect to d, and equating it to zero we obtain the value of d at which maxima occur for a reflection coefficient of unity as

$$d = (2n+1)\frac{\lambda}{4}, \tag{4-9}$$

where n is a positive integer and λ is the wavelength of the acoustic wave. For an SPL (re $20\ \mu Pa$) value of 120 dB, and a unity reflection coefficient, which corresponds to a maximum pressure of $2p_i$ occurring in the normal impedance tube, and for a frequency of $5\ kHz$, the density gradient at $\frac{\lambda}{4}$ is $0.016\ kg/m^3$.

The ratio of this density gradient fluctuation in the impedance tube to maximum detectable gradient of the system is 10^{-5}. Hence, it can be concluded that the density gradient fluctuation occupies only a minute fraction of the dynamic range of the device.

Static Calibration. In the absence of a knife-edge, the light intensity at the image plane is represented as $I_{\max}$ and, when fully blocked by the knife-edge, the intensity is 0, assuming that diffraction effects are negligible. Thus the light intensity varies from $0 - I_{\max}$. When the knife-edge blocks a part of the light, given by $a - k$ as seen in Figure 4.1, the intensity on the image plane is given by

$$I_{screen} = \frac{k}{a} I_{\max}. \tag{4-10}$$

When light is refracted due to the density gradient in the test section the expression for intensity is modified as

$$I = \frac{k + \Delta a}{a} I_{\max}, \tag{4-11}$$

where Δa is the knife-edge deflection as described in Chapter 2 and is given by Equation 2-29. From the above expression, the static sensitivity with respect to the deflection of the image at the knife-edge is given by

$$K = \frac{\partial I}{\partial \Delta a} = \frac{I_{\max}}{a}. \tag{4-12}$$

Since the light intensity is linearly related to the knife-edge deflection via Equation 4-11, a direct calibration can be done in an undisturbed (no-flow) case, by recording the light-intensity for several knife-edge positions ranging from no cutoff to full cutoff. The calibration curve which gives the voltage variation (directly proportional to the light intensity) vs knife-edge position can be used to determine the angular deflection of light rays that pass through a flow with a density gradient for a fixed knife-edge. In order to ensure that all the measurements are taken in the linear range, the schlieren system was operated at half cut-off, in which case the knife-edge blocks half the image of the source.

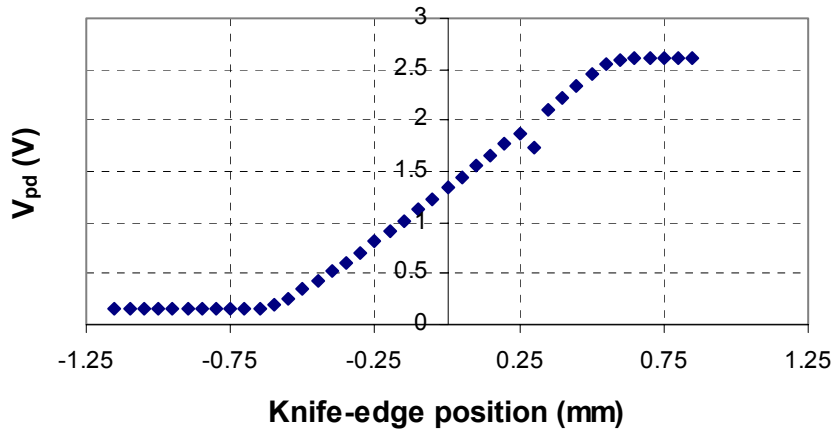

Figure 4-2: Knife-edge calibration of photodiode sensor.

A typical knife-edge calibration at the center of the image plane is shown in Figure 4-2. It shows the output voltage of the photo-detector as the knife-edge location is varied. The x-axis is rescaled so that the y axis passes through the operating point at half cutoff.

The source intensity variations with time are accounted for using a second reference photo-detector that measures the source intensity directly. Figure 4-3 shows the calibration curve after the photo-detector signal has been normalized using the reference detector signal. It can be seen that the temporal non-uniformity of the light

source shown in Figure 4-2 has been corrected by the reference photo detector in Figure 4-3.

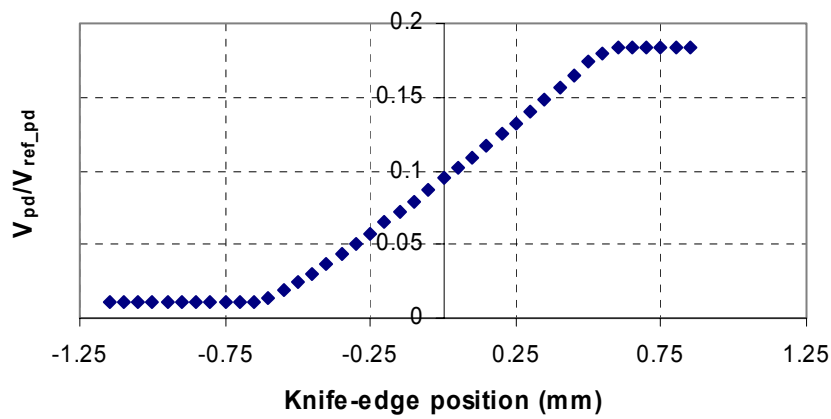

Figure 4-3: Photodiode knife-edge calibration.

The experiments also account for any zero offsets in the photo-detectors. A dimensionless parameter Φ is defined which takes into consideration the two corrections mentioned above.

$$\Phi = \frac{V_{pd} - V_{pd\_dark}}{V_{ref\_pd} - V_{ref\_pd\_dark}}, \tag{4-13}$$

where V_{pd} is the DC voltage of the photo-detector, V_{ref_pd} is the voltage of the reference photo-detector and V_{pd_dark} and $V_{ref\_pd\_dark}$ are the "no-light" voltage offset of the photo-detector and reference photo-detector, respectively. But, the equation does not take into consideration the spatial variation of light intensity in the image plane.

Calibration curves were obtained for three locations in the image plane as shown in Figure 4-4. The plots show the effect of non-uniform cut-off in the image plane. This leads to non-uniform illumination of the screen, which causes the slope (or static sensitivity) to vary from point to point in the image plane as can be seen in Figure 4-4. Non-uniform illumination also causes the maximum intensity to vary from one position

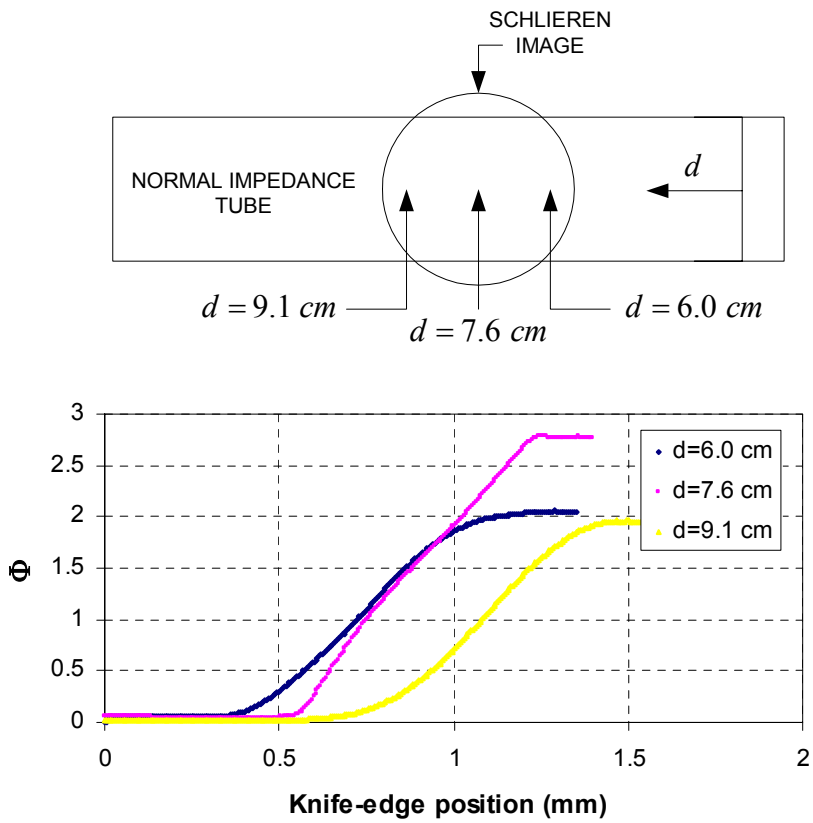

Figure 4-4: Photodiode knife-edge calibrations at three locations.

to another as can be seen in Figure 4-4. The second effect is not of major concern to us since the operating point is at the center of the curve and the intensity fluctuation is very small when compared to the linear range of the curve as shown in the beginning of this chapter.

The data were normalized using the equation

$$\Phi_{norm} = \frac{\Phi - \Phi_{\min}}{\Phi_{\max} - \Phi_{\min}}, \tag{4-14}$$

where $\Phi_{\min}$ and $\Phi_{\max}$ are the minimum and maximum value of Φ, respectively, at a particular location. This normalization allows us to compare slopes at the three locations, which otherwise have different linear ranges. Linear curve fits were obtained for the

linear portion of the curves using Excel Regression Tool as shown in Figure 4-5. The variation in the slope is clearly visible in the figure and was not found to fall within the 95% confidence interval of each other.

Figure 4-5: Linear region of the calibration curves at three locations after regression analysis.

It was determined that the non-uniform cut-off is mainly due to the finite filament size of the tungsten-halogen lamp. The condenser lens-slit combination could not produce uniform illumination over the entire area slit. This effect was mitigated by placing ground glass behind the rectangular slit.

Figure 4-6 shows the calibration curves at the three locations after the ground glass was inserted. It can be clearly seen from the plots that the variation in the slope of the curve (static sensitivity) is reduced considerably. This was verified using linear regression analysis.

The slope of the calibration curve is summarized in Table 4-1. It can be seen that there still exists a small variation in the slope. In the experiments conducted, since data was being taken only at twenty locations along the tube length, a calibration curve was found at each of the twenty locations and the local slope was used for data reduction.

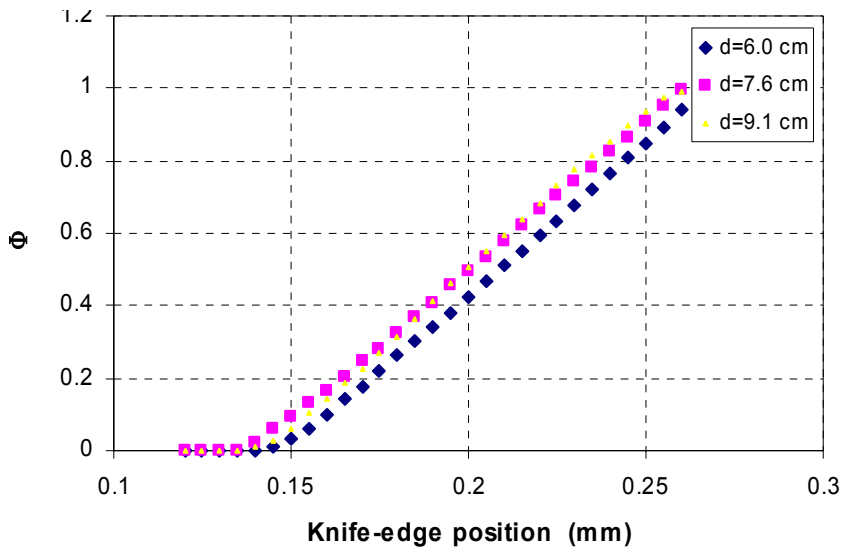

Figure 4-6: Calibration curves after the ground glass was inserted.

Table 4-1: Slope of the calibration curve at three different locations.

Location	**Slope (mm^{-1})**
Right	0.158 ± 0.001
Center	0.168 ± 0.002
Left	0.170 ± 0.001

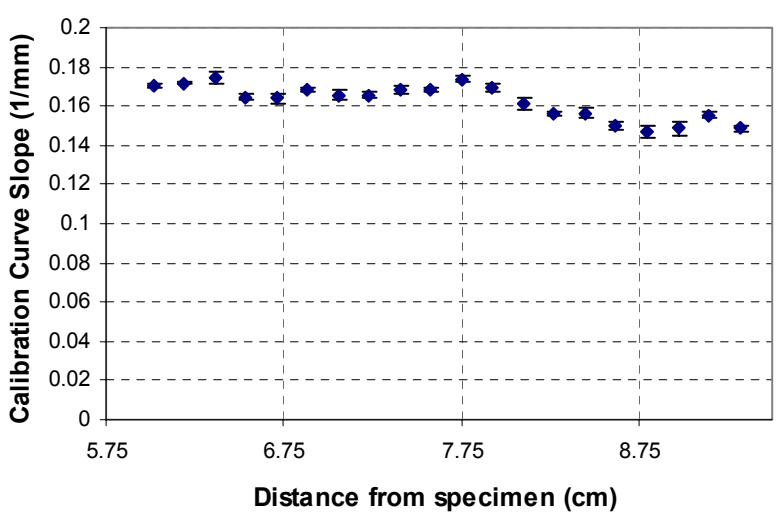

Figure 4-7: Slope of the calibration curve plotted along the test section.

The slope of the calibration curve at the twenty points taken prior to an experiment has been shown in Figure 4-7 with the 95% uncertainty estimates obtained from the linear regression analysis in Excel. The $x-axis$ gives the distance from the end of the normal impedance tube that contains the specimen.

The data reduction procedure for one location is now summarized. The dimensionless parameter, for a no-flow case is defined in Equation 4-13. For a case where there is light intensity fluctuation, this parameter is modified as

$$\Phi' = \frac{V_{pd} + V' - V_{pd\_dark}}{V_{ref\_pd} - V_{ref\_pd\_dark}} \tag{4-15}$$

where V' is the fluctuating term in the photo-detector signal caused by the acoustic density gradient in the impedance tube. The corresponding fluctuation element can be obtained by subtracting the undisturbed intensity (DC operating light intensity) from Equation 4-15 as

$$\Delta\Phi = \Phi' - \Phi = \frac{V'}{V_{ref\_pd} - V_{ref\_pd\_dark}} \tag{4-16}$$

4.2 Data Reduction Procedure

Optical deflectometry is based on the principle of a cross correlation between two points. This section briefly discusses the procedure followed to obtain the density gradient fluctuations

Calculation of Density Fluctuation. The fluctuation in light intensity is measured using a photo-detector mounted on a traverse in the image plane that moves along the length of the impedance tube. It has been shown in Chapter 2 that the fluctuation in light intensity is a measure of the refractive index or instantaneous density gradient in the direction normal to the knife-edge. This optical signal is converted to an electrical signal

using a photo-detector. The signal is then filtered and amplified using a filter/amplifier and digitized at high speed by a 16-bit A-D converter (National Instrument Model $NI4552$). The digitized data is transferred to a computer for subsequent analysis. A signal from a fixed microphone located at $d = 6.4\ cm$ is also sampled simultaneously. Using cross-spectral analysis, the coherent power in the photo-detector signal and the relative phase difference between the photo-detector signal and the microphone signal are determined.

The density fluctuation [12] can be represented as

$$\rho_x^{'}(x,t) = \mathrm{Re}\left|\frac{\partial \rho}{\partial x}(x)e^{i\omega t}\right|. \tag{4-17}$$

The spatially dependent term in the above equation is a complex quantity, which can be expressed as

$$\frac{\partial \rho}{\partial x}(x) = \left|\frac{\partial \rho}{\partial x}(x)\right| e^{i\phi(x)}. \tag{4-18}$$

The magnitude and the phase of the above equation are determined by a cross-spectral analysis described below.

The frequency response function between the input microphone signal x and output photo detector signal y is defined as [19]

$$H = \frac{G_{xy}}{G_{xx}} = \frac{|G_{xy}|}{G_{xx}} e^{i\Theta} = |H| e^{i\Theta}, \tag{4-19}$$

where G_{xy} is the cross spectrum between the input and the output signal, and G_{xx} is the auto spectrum of the input signal.

The voltage fluctuation detected by the photo-detector at any location can be represented as

$$V'(x,\omega) = \mathrm{Re}\left[\left|V'(x)\right| e^{i\phi(x)} e^{i\omega t}\right], \tag{4-20}$$

and the reference microphone signal at a distance d_1 in the plane-wave tube is given by

$$P(d_1,\omega) = \mathrm{Re}\left[\left|P(d_1)\right| e^{i\psi(d_1)} e^{i\omega t}\right]. \tag{4-21}$$

In Equation 4-19, the magnitude $|H|$ is the ratio of the output to the input signal, and the phase $\Theta(x) = \phi(x) - \psi(d_1)$ is the phase difference between the output and input signals.

The amplitude of $P(d_1,\omega)$ is obtained from the power spectrum, $P_{rms}^2(d_1,\omega)$, of the microphone signal and the phase ψ at d_1 with respect to $d = 0$ using two-microphone method. These values are then used to compute the amplitude and phase distribution of the voltage fluctuations.

The calculated amplitude of $V'(x,\omega)$ is then substituted in Equation 4-16 to obtain the corresponding values of $\Delta\Phi$. The slope of the calibration curve can be written as

$$slope = \frac{\Delta\Phi}{\Delta a} \tag{4-22}$$

where $\Delta\Phi$ is related to the fluctuating element of the light intensity and Δa is the shift in the light rays in the plane of the knife-edge, which causes the light intensity fluctuation.

Using the slope of the calibration curve at the corresponding location, the shift in light ray Δa is obtained using Equation 4-22. Subsequently, the angular deflection ε_x corresponding to the magnitude of light intensity fluctuation can be obtained using Equation 2-29. Finally, the density gradient is obtained by substituting ε_x in Equation 4-1.

The data reduction procedure described above was automated using a MATLAB code for all the locations, and the density gradient distribution (magnitude and phase) are determined along the length of the tube. A schematic of the data reduction procedure is shown in Figure 4-8.

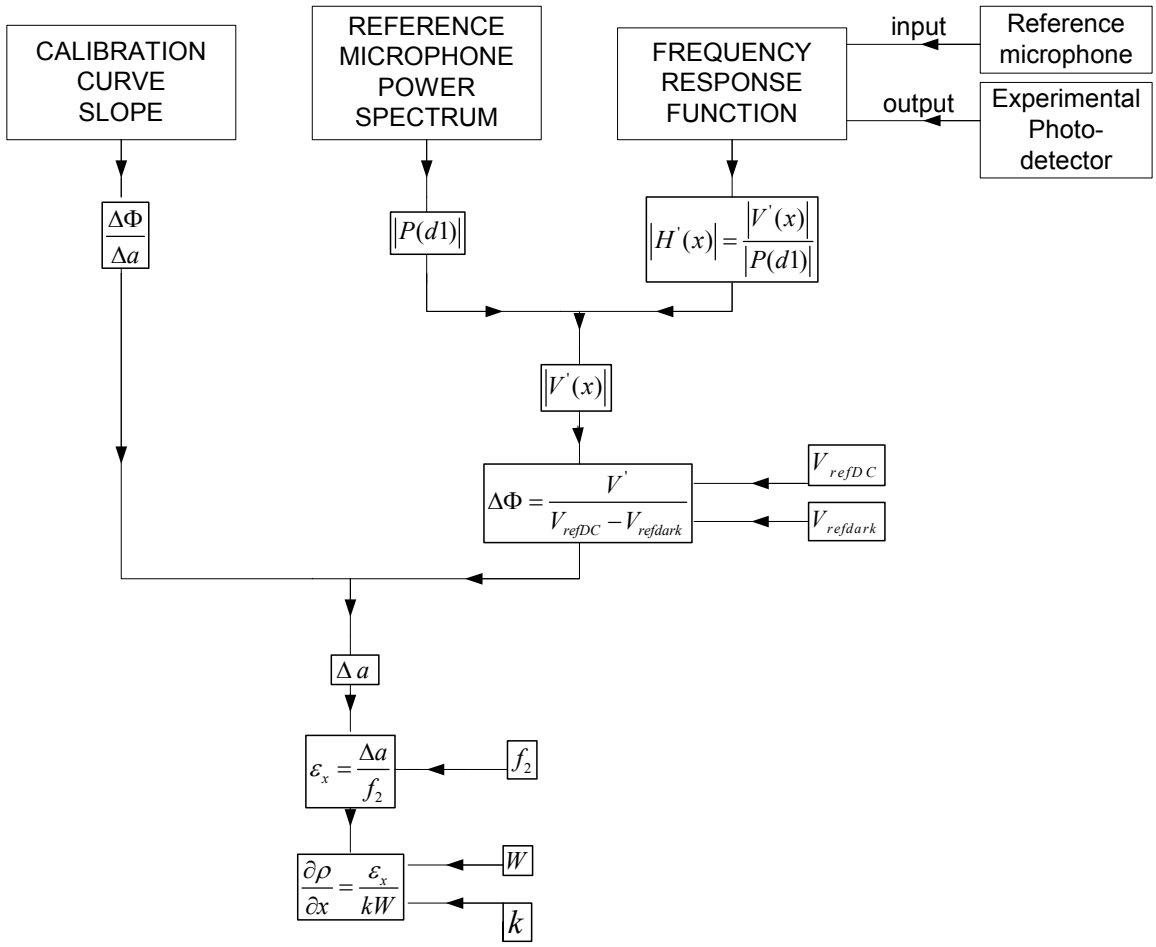

Figure 4-8: Data reduction procedure.

Further, frequency domain correlation tools, such as coherence and coherent power spectrum are used. The ordinary coherence function for x as input signal and y as output signal is defined as

$$\gamma_{xy}^2 = \frac{|G_{xy}|^2}{G_{xx}G_{yy}}. \tag{4-23}$$

The coherence function is related to the portion of y that is linearly correlated to the input signal x. The coherence power spectral density is defined as

$$G_{yy,coh} = \gamma^2 G_{yy}. \tag{4-24}$$

It is a direct measure of the power-spectral density that is linearly coherent with the reference pressure. These two parameters help determine the quality of the frequency response measurements.

4.3 Dynamic Calibration

The dynamic system sensitivity of the system was determined after the completion of the impedance tube experiments. The reflected output from a laser pulse was directed towards the photo-detector at the operational gain of the system.

The pulse input duration was found to be much shorter ($\approx 20\ n\text{sec}$) than the photo-detector system time constant. Hence, the input was treated as an impulse. Figure 4-9 shows the measured impulse response of the photo-detector.

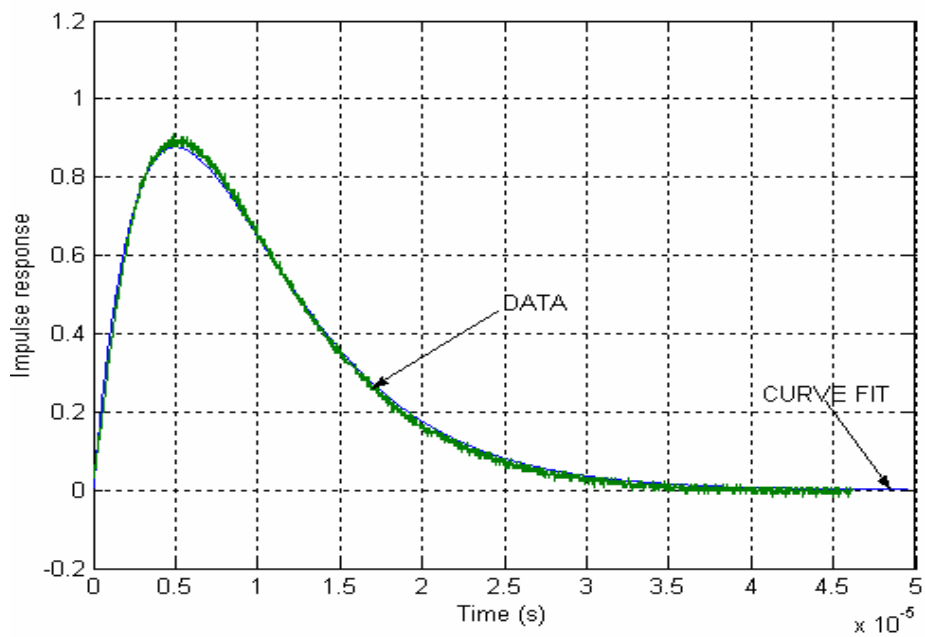

Figure 4-9: Impulse response of the experimental photo-detector.

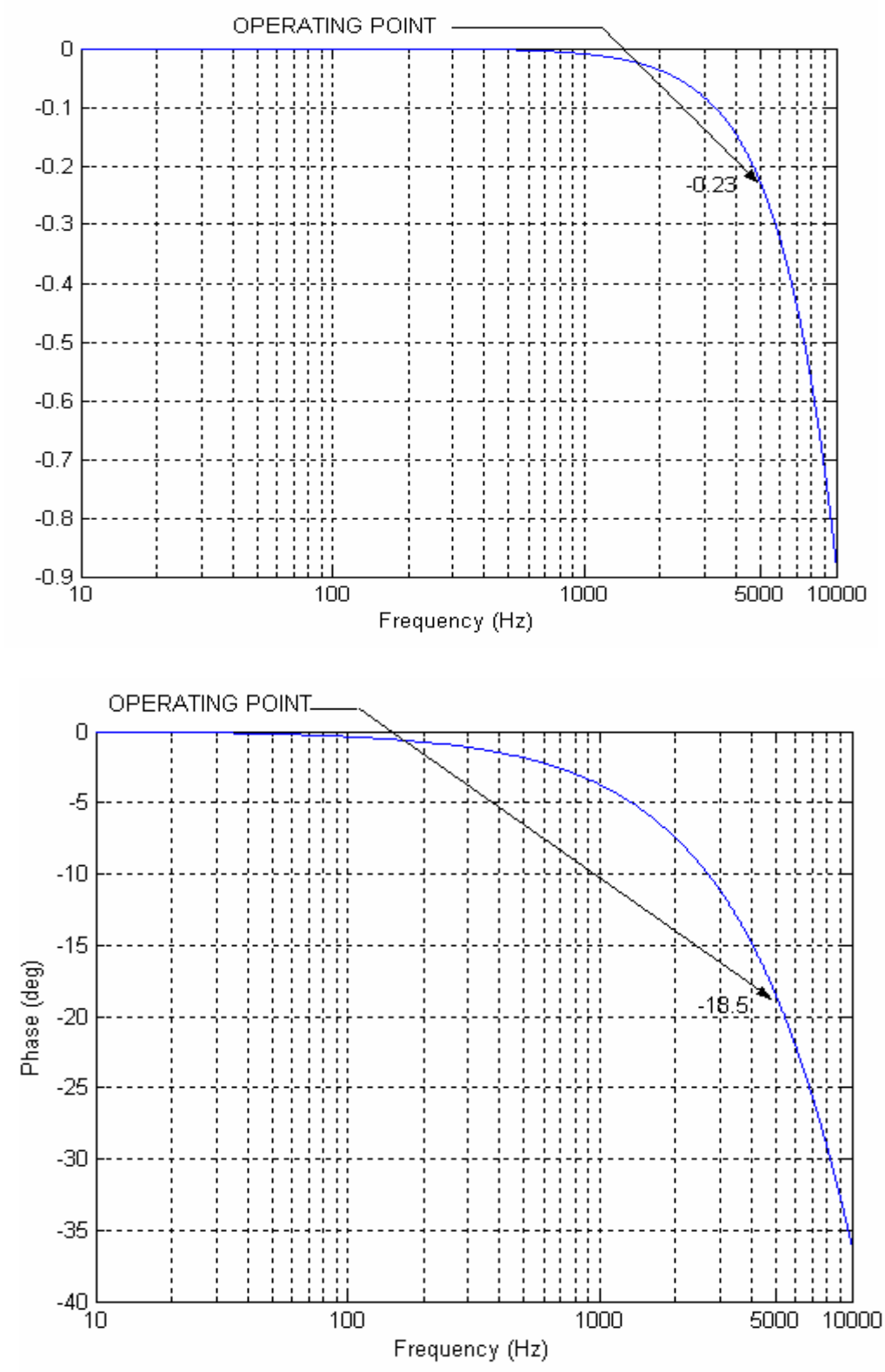

Figure 4-10: Frequency response of the experimental photo-detector at the experimental gain setting.

The impulse response shows that the system behaves like an over damped second-order system. A curve fit was performed using the equation

$$h(t) = \frac{K}{2\omega_n\sqrt{\xi^2 - 1}}\left[e^{-\omega_n(\xi-\sqrt{\xi^2-1})t} - e^{-\omega_n(\xi+\sqrt{\xi^2-1})t}\right], \tag{4-25}$$

where ξ is the damping ratio, ω_n the undamped natural frequency and K is related to the strength of the pulse. The damping ratio was found to be 1.0018 and $\omega_n = 1.93\times10^5\ rad/\sec$. Since it is an over-damped second-order system, it can be concluded that there is a time delay and an amplitude attenuation.

The frequency-response characteristics obtained from the damping ratio and the undamped natural frequency are shown in Figure 4-10. The gain variation was found to be $-0.2\ dB$ and the phase lag -18.5^0 at $5\ kHz$. From the response, it can be seen that while the gain is negligible, the phase lag has a finite value. This was accounted for while reducing the data in Chapter 5.

4.4 Experimental Procedure

Two experimental methods were employed simultaneously to investigate the density gradient fluctuations in the normal impedance tube: the optical deflectometer and the two-microphone method [25].

The entire experimental procedure was automated using a LabVIEW program. The program simultaneously acquired data from two photo-detectors and two microphones, controlled a 2-D traverse and partially processed the data. Data was acquired at twenty different locations with a spacing of $1.7\ mm$ across the schlieren image.

At each location, the filtered fluctuating signal of the experimental photo-detector and the pressure fluctuation signals from two microphones placed at a distance

$d_1 = 6.4\ cm$ and $d_2 = 4.5\ cm$ from the specimen, respectively, were acquired. The dc component of the experimental and the reference photodector were acquired using a digital multimeter (Keithley model 2400).

For the deflectometer, the frequency response function with the first microphone signal (reference microphone) as input and experimental photo detector signal as output is calculated simultaneously by the LabVIEW program. The DC component of the photo-detector signals is used to correct the temporal non-uniformity in light source as discussed in section 4.1.

For the two-microphone method, signals from the two microphones were used to constructing the standing wave pattern in the impedance tube. The reflection coefficient is calculated using Equation 2-10 by the program as the data is acquired.

The analysis was carried out entirely in the frequency domain and ensemble averaging was performed over $10,000$ blocks of data with 1024 data points in each block. Uncorrelated noise is reduced by ensemble averaging. Thus the random noise variations in the spectrum are smoothed out. The sampling frequency of the data acquisition system was set at $102400\ samples/\sec$ and hence Δf was $100\,Hz$. Since the signals were periodic, a rectangular widow was applied and spectral leakage was avoided [19].

Once the entire procedure was completed, the static calibration was repeated. It was observed that the variation in the slope of the calibration curve at a particular location was negligible during the course of the experimental procedure. The traverse was moved to the adjacent location. Static calibrations were performed at the next location, and the measurement procedure was repeated for all twenty locations.

CHAPTER 5
RESULTS AND DISCUSSION

This chapter presents the theoretical, computational, and experimental results obtained during the course of the research. The results obtained from two experimental methods with the uncertainty estimates are compared in the latter part of the chapter.

5.1 Theoretical Results

Prior to the experiments, the variations in pressure, density, and density gradient were calculated along the length of the impedance tube. Since the experiments were being conducted for a sound hard termination, the value of R should ideally be unity and was thus used for these calculations. From Equation 2-3 pressure distribution for $R = 1$ is

$$p(d) = p_i(\mathrm{e}^{ikd} + \mathrm{e}^{-ikd}). \tag{5-1}$$

From Equation 2-13, the density distribution can be obtained as

$$\rho(d) = \frac{p_i}{c^2}(\mathrm{e}^{ikd} + \mathrm{e}^{-ikd}). \tag{5-2}$$

And using Equation 2-15, the density gradient for $R = 1$ is derived as

$$\frac{\partial \rho}{\partial d} = \frac{p_i jk(e^{jkd} - e^{-jkd})}{c^2}. \tag{5-3}$$

Figure 5-1 provides a comparison of pressure, density and density gradient fields. It can be seen that pressure doubling occurs at $d = 0, \frac{\lambda}{2}, \lambda, ...$ and pressure nodes occur at

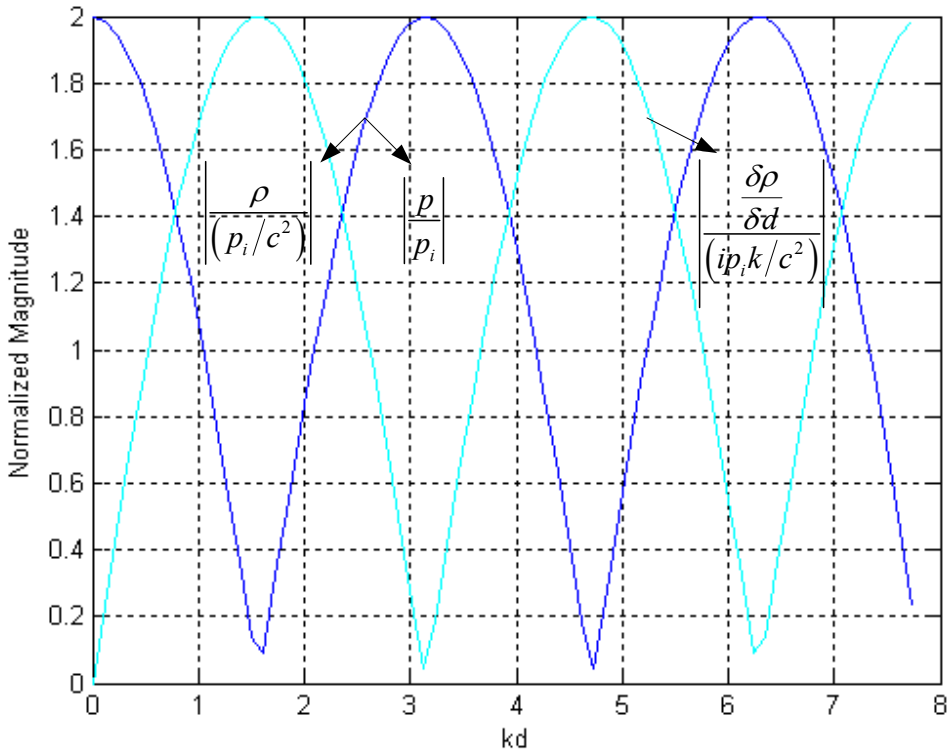

Figure 5-1: Comparison of pressure, density and density gradient distributions.

$d = \frac{\lambda}{4}, \frac{3\lambda}{4}, \frac{5\lambda}{4}, \ldots$. Also, from the figure it can be observed that the nodes of the pressure wave correspond to the maxima of the density gradient and vice versa.

The variation in the phase of pressure and density gradient with respect to kd for $R = 1$ is shown in Figure 5-2. A 180 degree shift phase occurs at $d = \frac{\lambda}{4}, \frac{3\lambda}{4}, \frac{5\lambda}{4} \ldots$ in the case of the pressure distribution and, at $d = 0, \frac{\lambda}{2}, \lambda, \frac{3\lambda}{2} \ldots$ in density distribution.

In practice, however, leaks/losses exist in the impedance tube and, hence, the magnitude and phase of the reflection coefficient were calculated using the two-microphone method as discussed in Chapter 2.

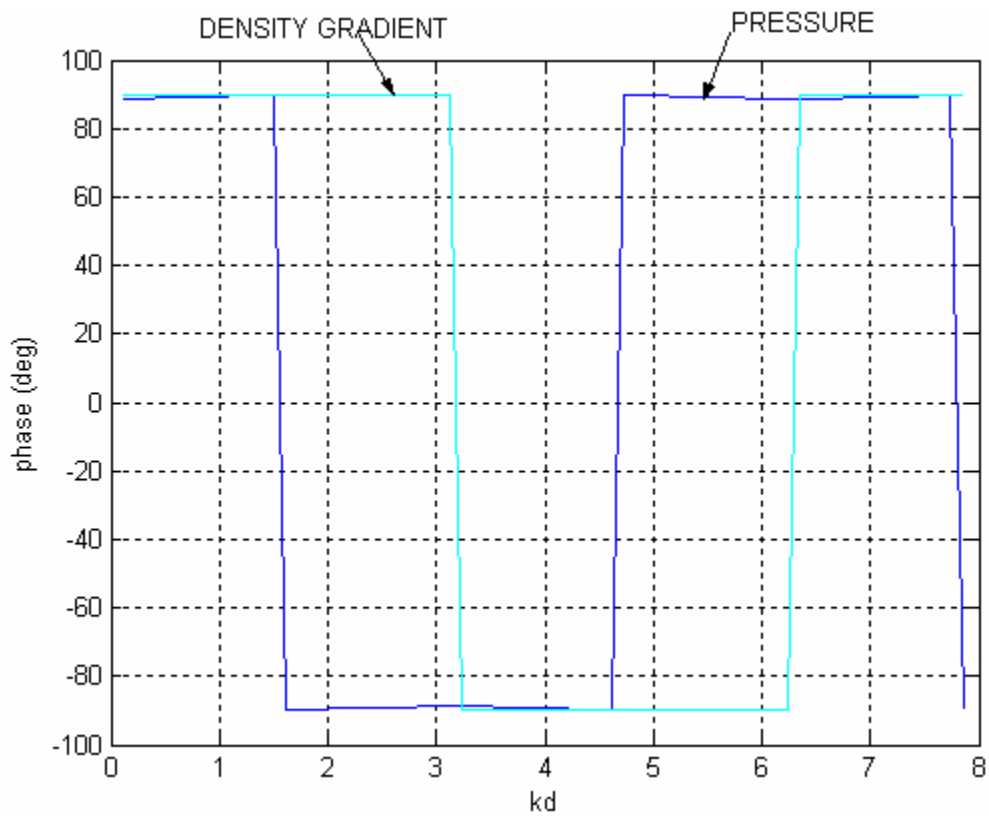

Figure 5-2: Phase variation for a rigid termination.

The density gradient distribution in the impedance tube can be obtained using the pressure signals at two locations, d_1 and d_2 (see Figure 2-1), using the following procedure. The amplitude of the pressure signal (Appendix D) is derived from Equation 2-3 as

$$|p(d)| = A\sqrt{(\cos(k(d-l)) + |R|\cos(\phi_r - kd - kl))^2 + (\sin(k(d-l)) + |R|\sin(\phi_r - kd - kl))^2}, \tag{5-4}$$

where l is the length of the impedance tube, d is the distance from the test specimen, $|R|$ and ϕ_r are the magnitude and phase of the reflection coefficient, respectively. Substituting the pressure magnitude at a location d_1 in Equation 5-4, the constant A is determined. This value can then be verified by using the pressure amplitude at location d_2. The density gradient amplitude is derived from Equation 2-15 as

$$\left|\frac{\partial\rho}{\partial x}(d)\right| = \frac{Ak}{c^2}\sqrt{(\cos(k(d-l)) - |R|\cos(\phi_r - kd - kl))^2 + (-\sin(k(d-l)) + |R|\sin(\phi_r - kd - kl))^2}. \tag{5-5}$$

The density gradient amplitude for a known value of A and reflection coefficient is thus obtained vs. position along the length of the tube using the above expression. The phase of the density gradient is found from Equation 2-15

$$\theta = \tan^{-1}\left[\frac{(\cos(k(d-l)) - |R|\cos(\phi_r - kd - kl))}{(-\sin(k(d-l)) + |R|\sin(\phi_r - kd - kl))}\right]. \tag{5-6}$$

The magnitude and phase of the density gradient will be used to verify the experimental results obtained from the deflectometer in Section 5.3.2.

5.2 Numerical Results

Data analysis similar to the test conditions was performed for simulated pressure waves. The pressure across the plane wave tube at a particular position at a particular instant of time is given by

$$p = \mathrm{Re}\left[A\,\mathrm{e}^{-ikl}\left(\mathrm{e}^{ikd} + \mathrm{R}\,\mathrm{e}^{-ikd}\right)\mathrm{e}^{iwt}\right], \tag{5-7}$$

where k is the wave number, l is the length of the tube, R is the complex reflection coefficient and ω is the frequency of the signal. A reference signal was taken at the origin, $kd = 0$. Cross-spectral analysis of the signal at various locations with respect to this reference signal was then performed. Pressure signals were reconstructed using the amplitude and phase information. The resulting animation consists of 72 frames (i.e., the phase is advanced by 5 deg. between frames).

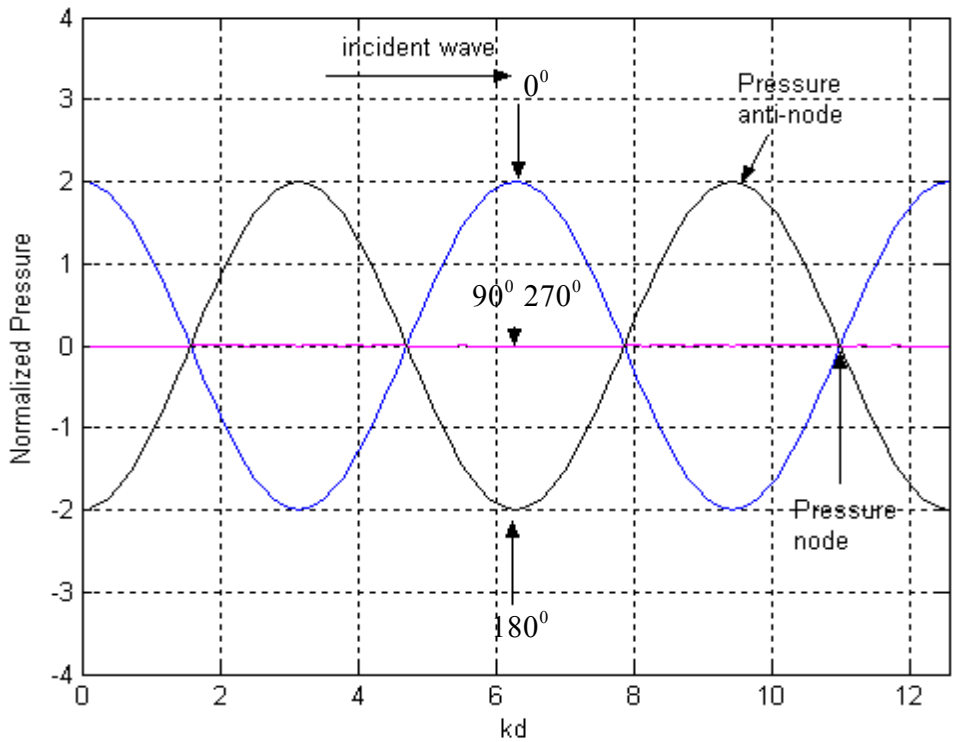

Figure 5-3: Pressure waves at various phases for R = 1.

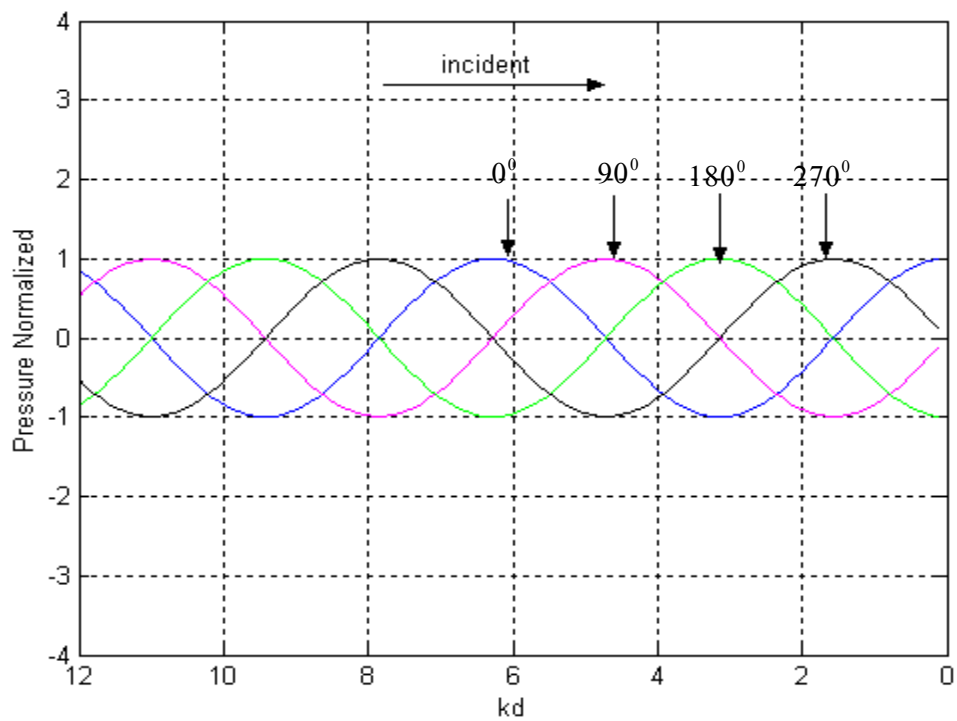

Figure 5-4: Pressure waves at various phases for R = 0.

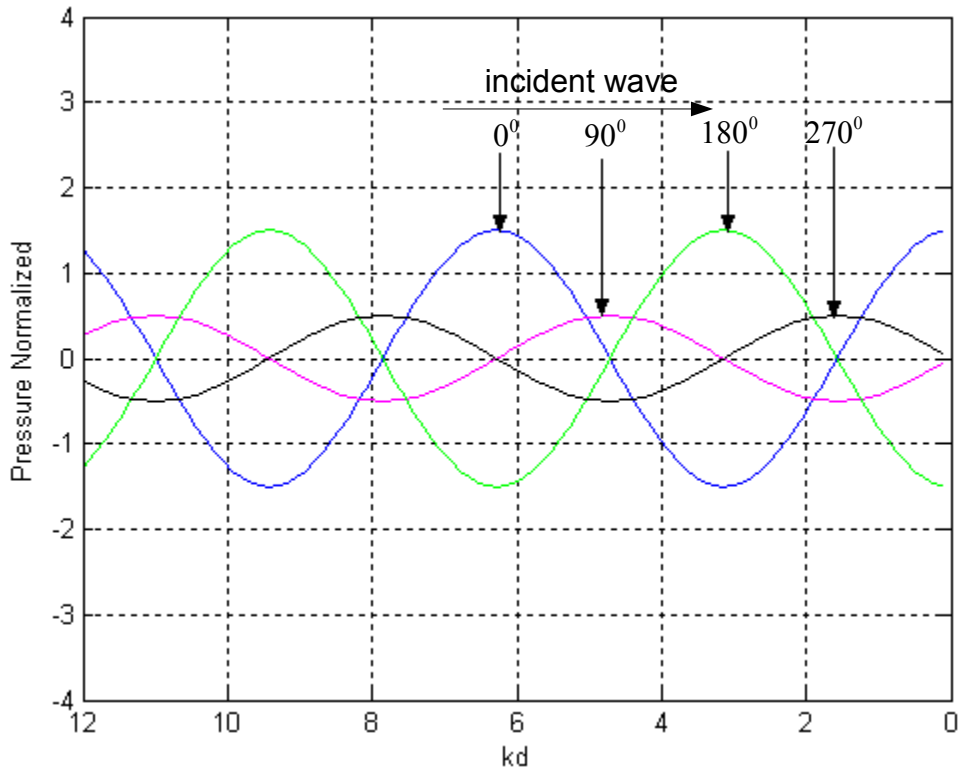

Figure 5-5: Pressure waves at various phases for R = 0.5.

Phase locked movies for various values of R were obtained. Except for $R = 0$, standing wave patterns exist. Figure 5-3 shows sample snapshots of the movie for $R = 1$ case. This represents a rigid termination or sound-hard boundary condition. Pressure doubling occurs at the interface $kd = 0$ and the pressure reduces to zero at the nodes. The termination acoustic impedance defined by Equation 2-6 is infinite. Also, the standing wave ratio is infinite [18].

A purely progressive pressure wave in a tube with a ρc termination is shown in Figure 5-4. It can be seen that a standing wave does not exist for $R = 0$. The pressure waves propagate towards the open end of the tube as the phasor is increased from 0° to 270°.

Simulations were also obtained for a general resistive termination (see Figure 5-5). The value of reflection coefficient was taken to be $\frac{1}{2}$. The standing wave ratio is 3 and $Z_n = 3Z_0$.

5.3 Experimental Results

As mentioned in Chapter 4, two experimental methods were employed simultaneously to investigate the density gradient fluctuations in the plane-wave tube: the optical deflectometer and the two-microphone method. This section describes the results obtained from the experiments conducted. In particular, the results obtained using these two methods are compared later in this section.

5.3.1 Measurement of Density Gradient Using the Optical Deflectometer

An experimental set-up as described in Chapter 2 was constructed. Light intensity fluctuations were measured along the length of the test section using a photo detector mounted on a traverse. Pressure waves were generated at $5\ kHz$ in the plane-wave tube.

The noise floor of the detector for a no-light case was determined and expressed as power spectral density in Figure 5-6. The power spectra of the detector for light-on cases, with various values of the gain are plotted in Figure 5-7. The power spectrum of the detector was seen to increase, as the gain was varied from 0 to 0.4.

Beyond this gain, the power spectrum reduced steeply and remained closer to the 0 gain spectrum. This is likely due to the saturation of the photo-detector. Hence the operating amplifier gain was set at 0.35.

Figure 5-8 and Figure 5-9 show examples of photodiode and microphone spectra, respectively, at $145.4\ dB$. These spectra were measured for illustrative purpose using Virtual bench. The dominance of power at $5\ kHz$ is clearly visible from both the plots.

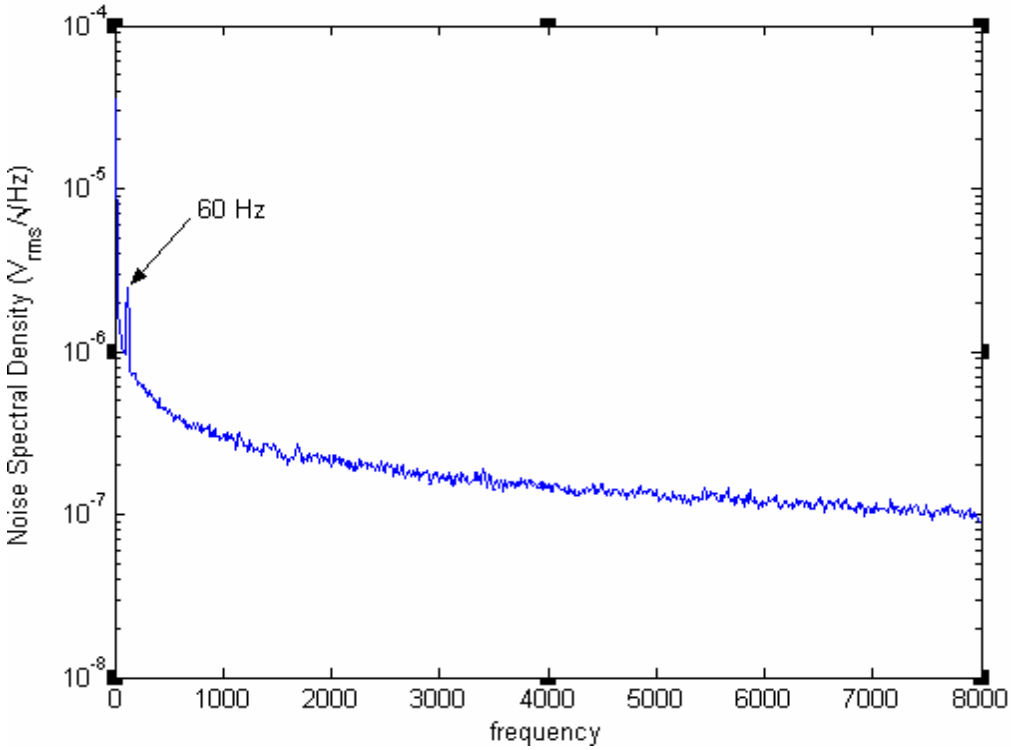

Figure 5-6: Noise floor of the experimental photo-detector at an operational gain of 0.35.

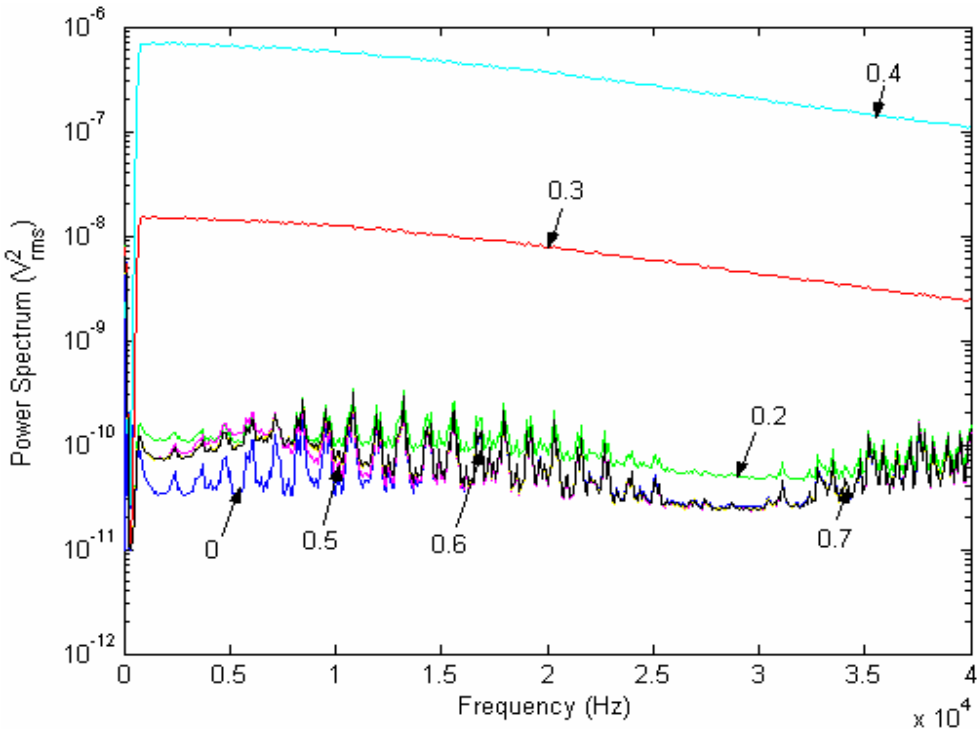

Figure 5-7: Noise floor of the experimental photo-detector (light-on) for various gains.

Figure 5-10 shows the coherence between the photo-detector and the reference microphone signal. Although the coherence value is low (0.19) at the operating frequency, the coherent power of the photo-detector at $5\ kHz$ is approximately three orders-of-magnitude above the noise floor (Figure 5-11).

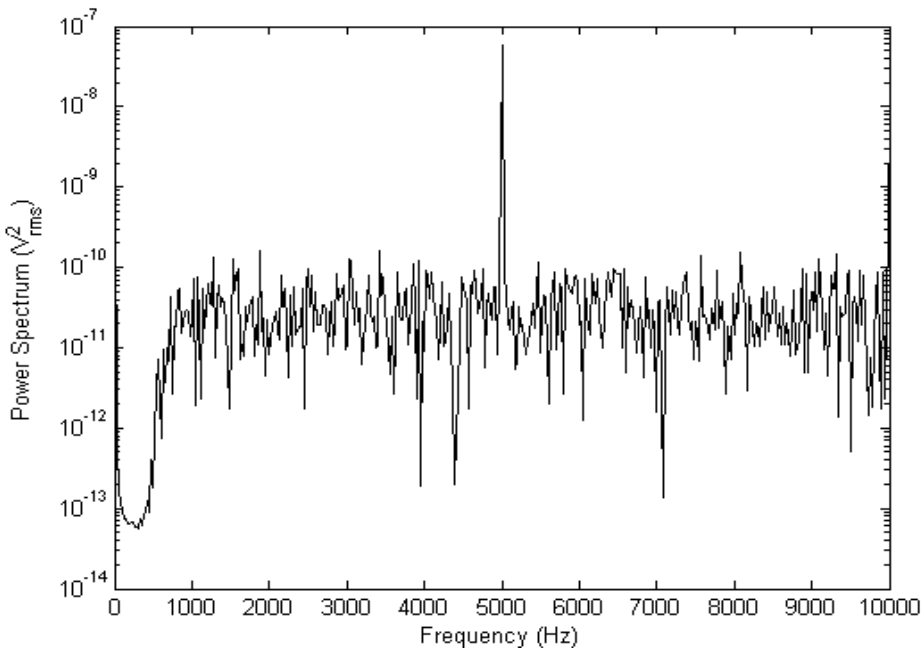

Figure 5-8: Example of photo-detector power spectrum at $145.4\,dB$.

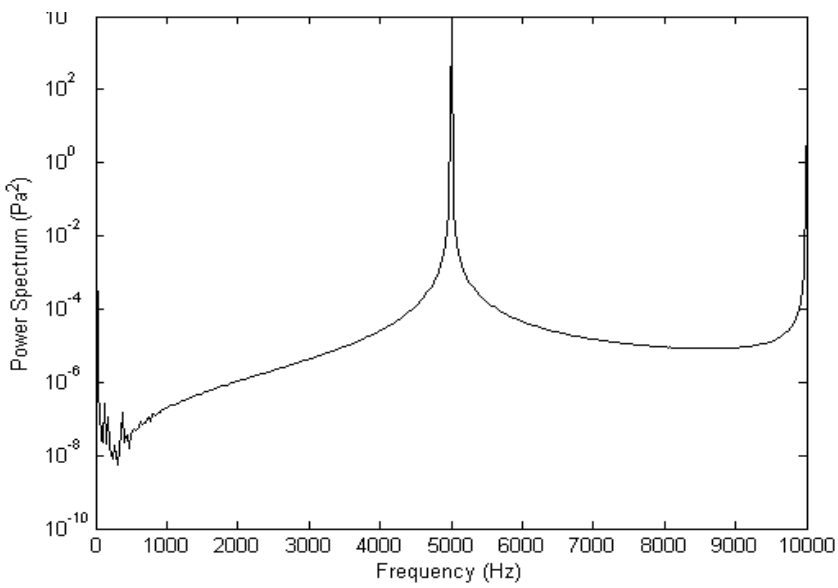

Figure 5-9: Example of reference microphone power spectrum at $145.4\,dB$.

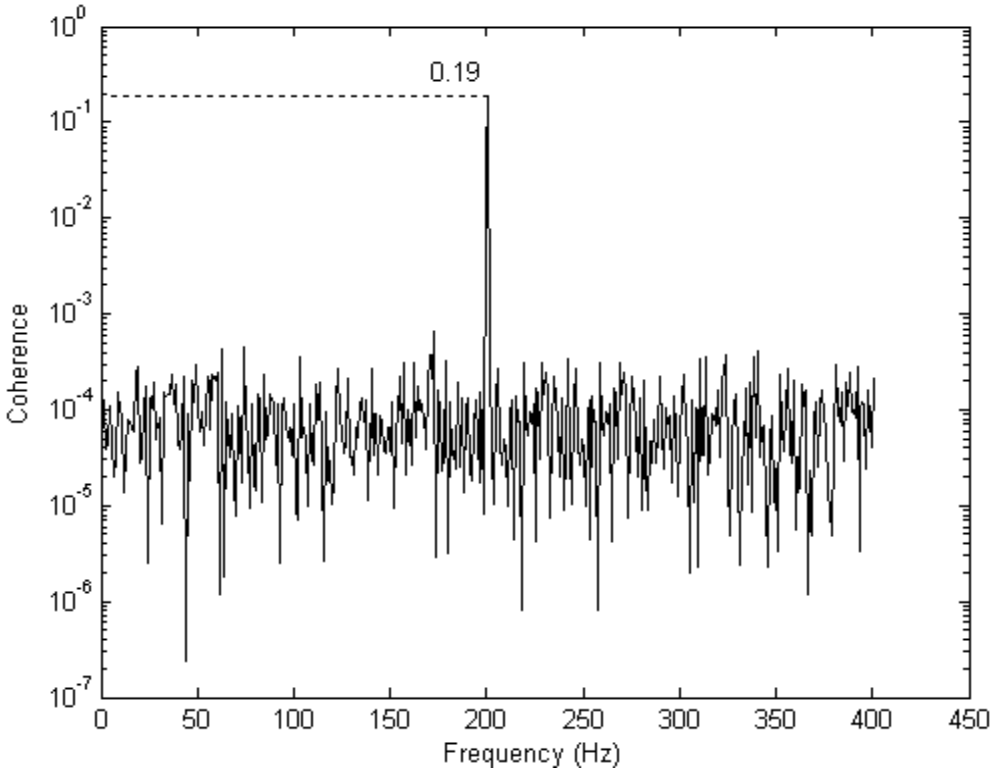

Figure 5-10: Example of coherent spectrum at 145.4 dB .

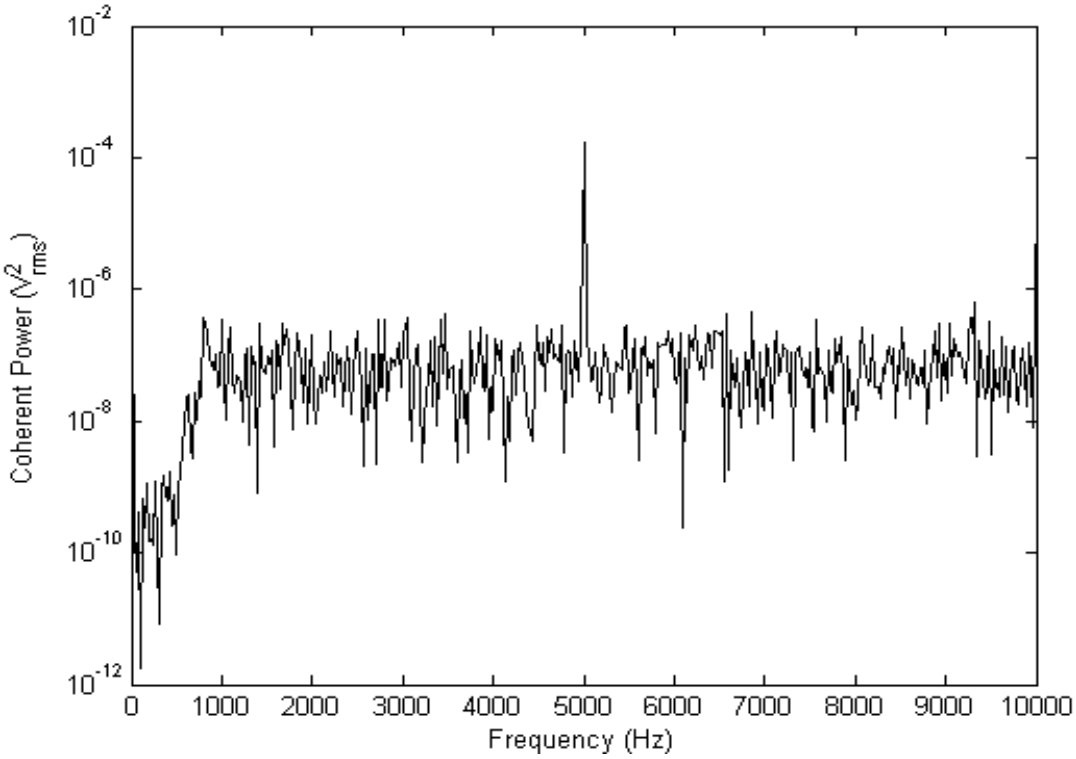

Figure 5-11: Example of photo-detector coherence power at 145.4 dB .

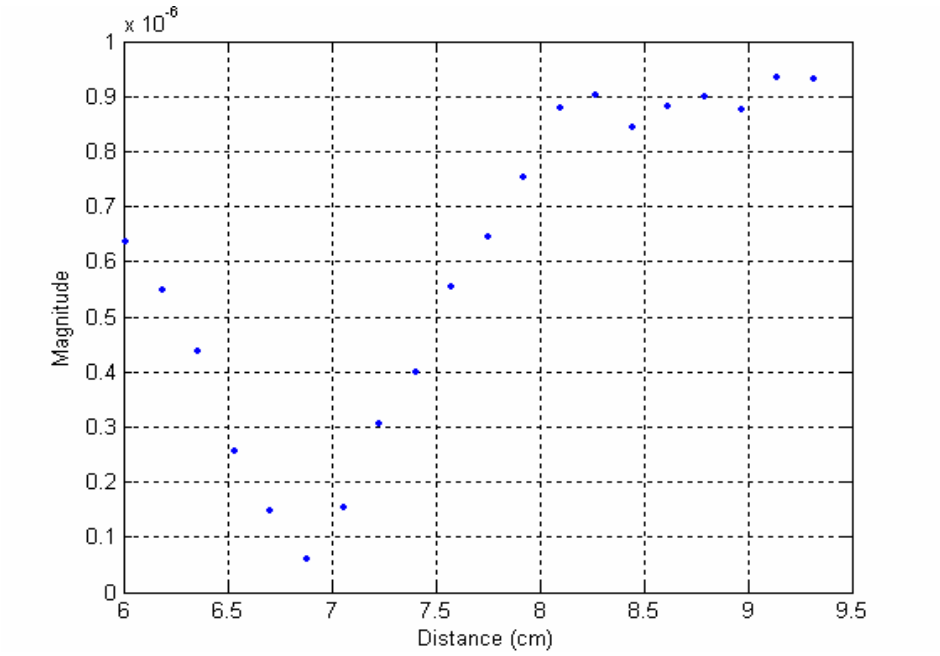

Figure 5-12: Magnitude of the frequency response function at 145.4 dB .

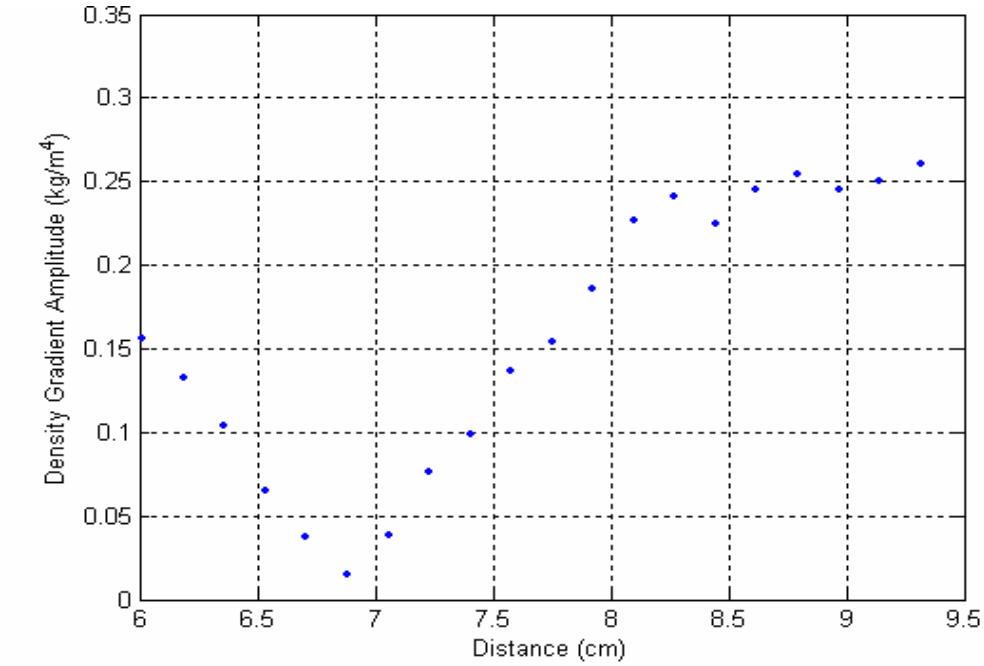

Figure 5-13: Density gradient amplitude along the length of the tube at 145.4 dB .

Light intensity fluctuations were measured at 20 equally spaced locations. The frequency response function gain has been plotted in Figure 5-12. Data was reduced according to the procedure described in Chapter 4, and the density gradient distribution was obtained in the impedance tube and is shown in Figure 5-13. The density gradient distribution reveals a standing wave pattern and follows the trend discussed in Section 5.1.

Data was acquired for Sound Pressure Levels ranging from $123-155\ dB$. From Figure 5-14, for example, the power of the photo-detector signal at the operating frequency is close to the noise floor at $126.4\ dB$. Also, at low SPL, the coherence of the signal reduced considerably, the coherence at $126.4\ dB$ was 0.0009.

Nevertheless, the coherent power at $5\ kHz$ was still dominant (Figure 5-16). The density gradient distribution at $126.38\ dB$ is shown in Figure 5-18.

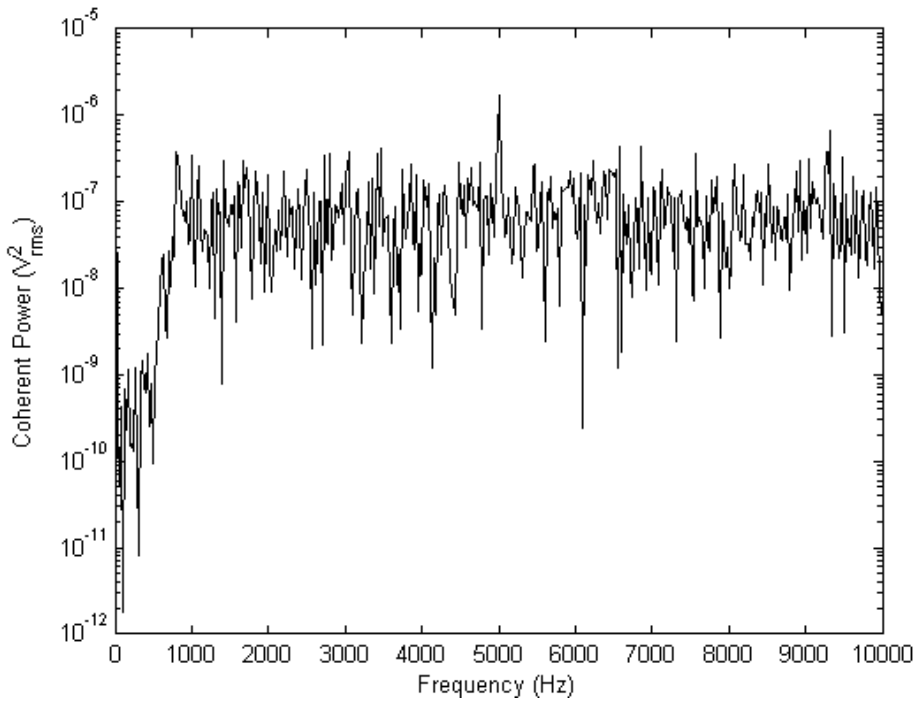

Figure 5-14: Example of photo-detector power spectrum at $126.4\,dB$.

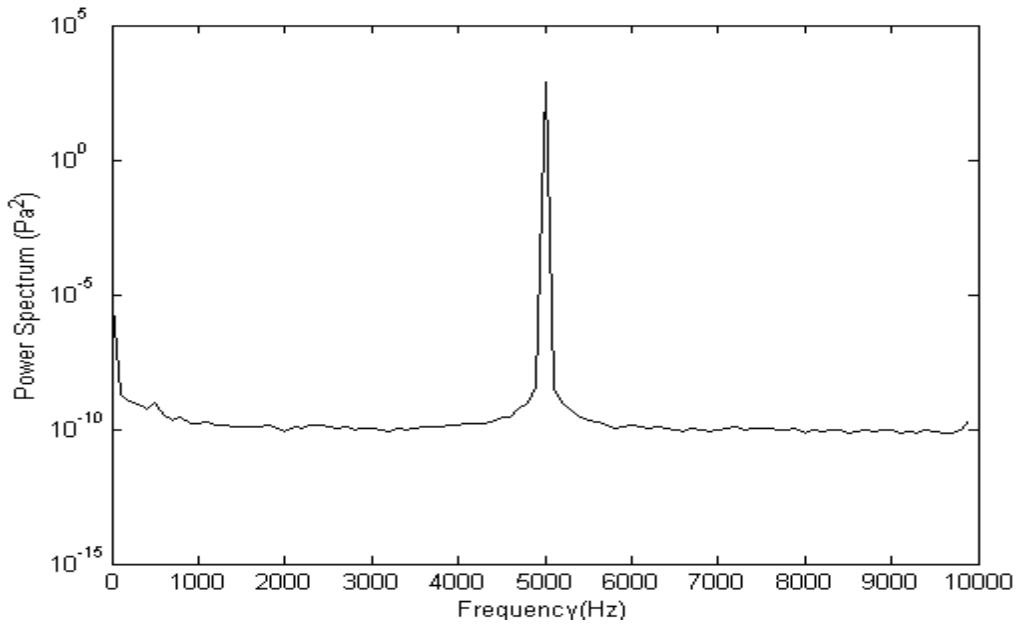

Figure 5-15: Example of reference microphone power spectrum at 126.4 dB .

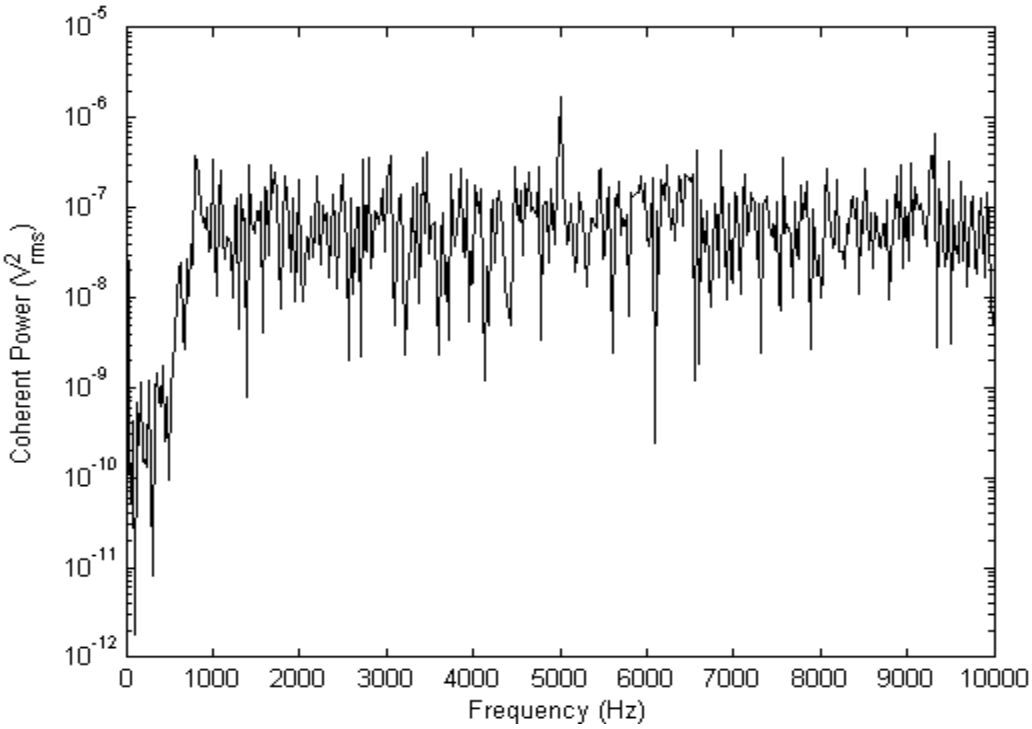

Figure 5-16: Coherent power of the photo-detector at 126.4 dB .

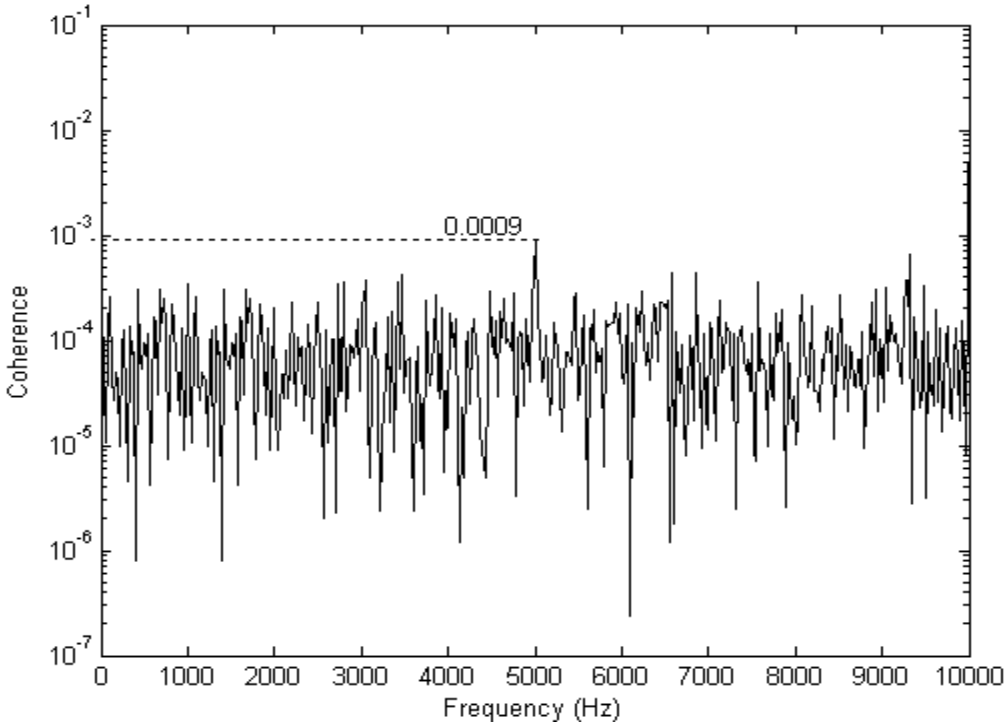

Figure 5-17: Example of coherence spectrum at $126.4\,dB$.

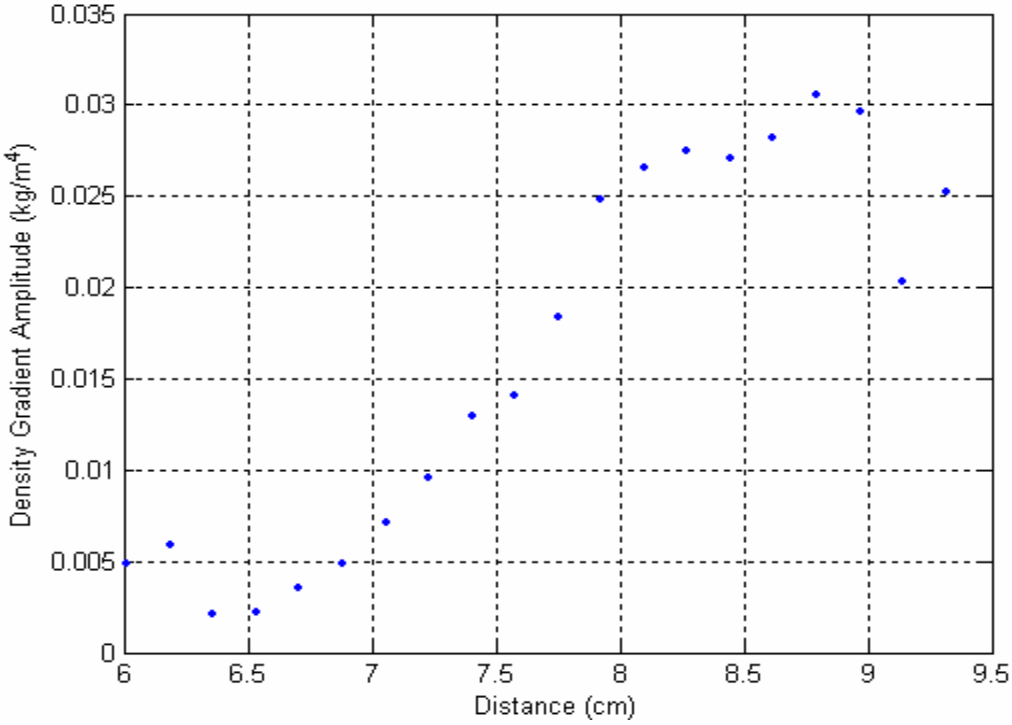

Figure 5-18: Density gradient amplitude along the length of the tube at $126.4\,dB$.

The phase difference between the photo-detector signal and the microphone signal is obtained from the frequency response function (Figure 5-19). The phase is found to remain constant with a 180^0 shift at the density-gradient node. To obtain the absolute value of the phase of the density gradient, we require the phase information of the reference signal, which is obtained from the two-microphone method in Section 5.3.2.

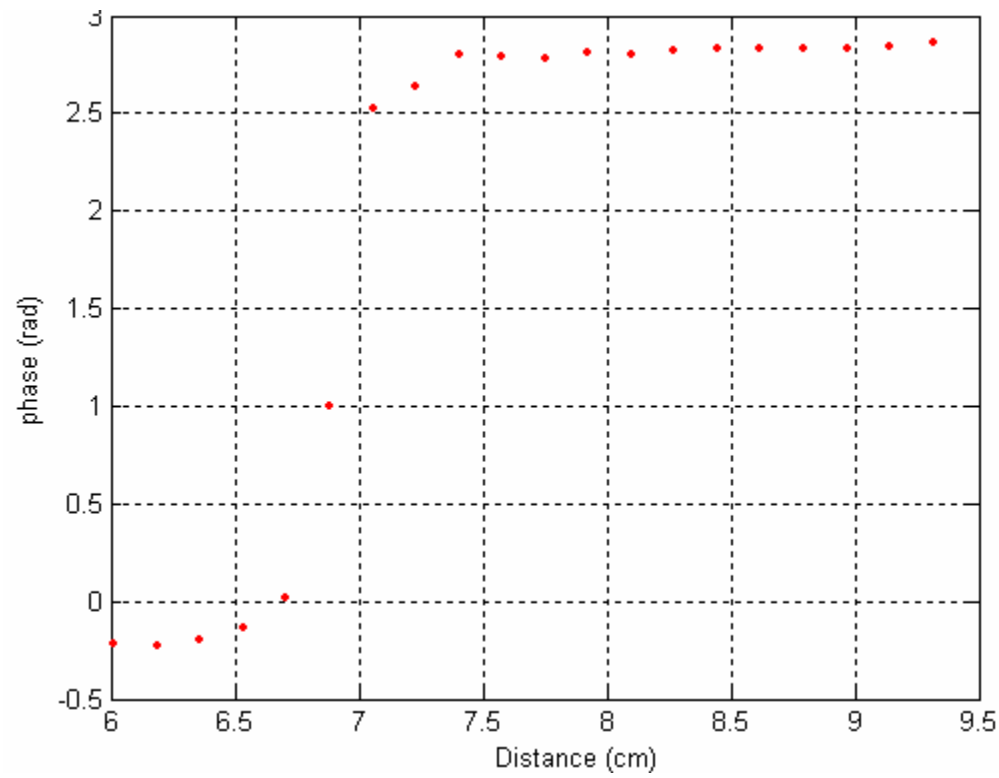

Figure 5-19: Phase difference between the photo-detector signal and the reference microphone signal at $145.4\,dB$.

5.3.2 Measurement of Density Gradient Using microphones

The density gradient along the normal impedance tube length was calculated as described in section 5.1. The amplitude of the pressure signal at a distance $4.5\ cm$ and $6.4\ cm$ is obtained from the power spectrum of the microphone signals.

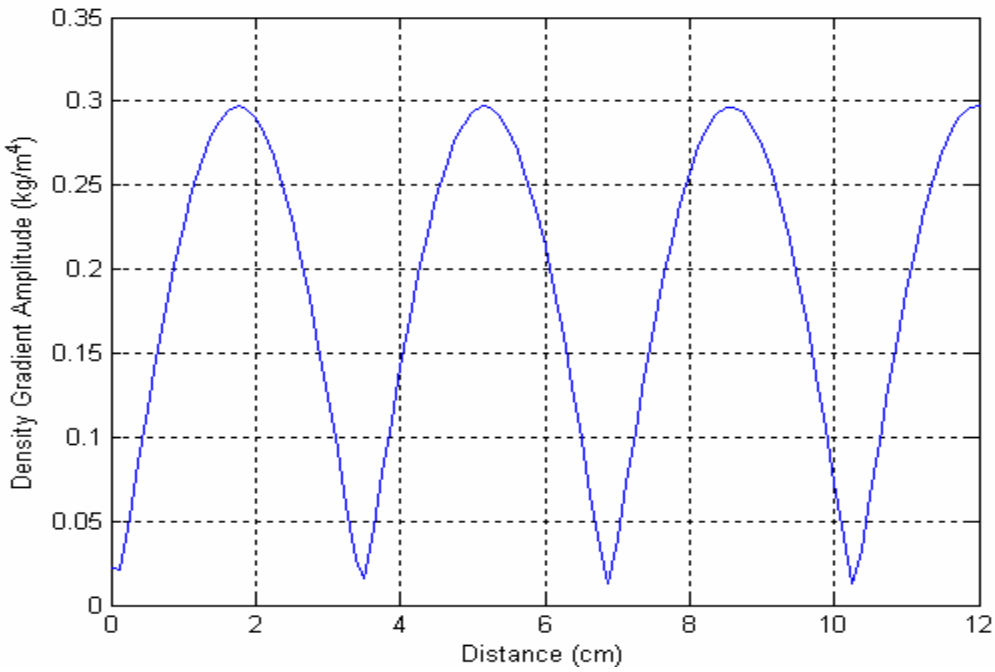

Figure 5-20: Density gradient amplitude along the length of the tube using the microphone method at $145.4\,dB$.

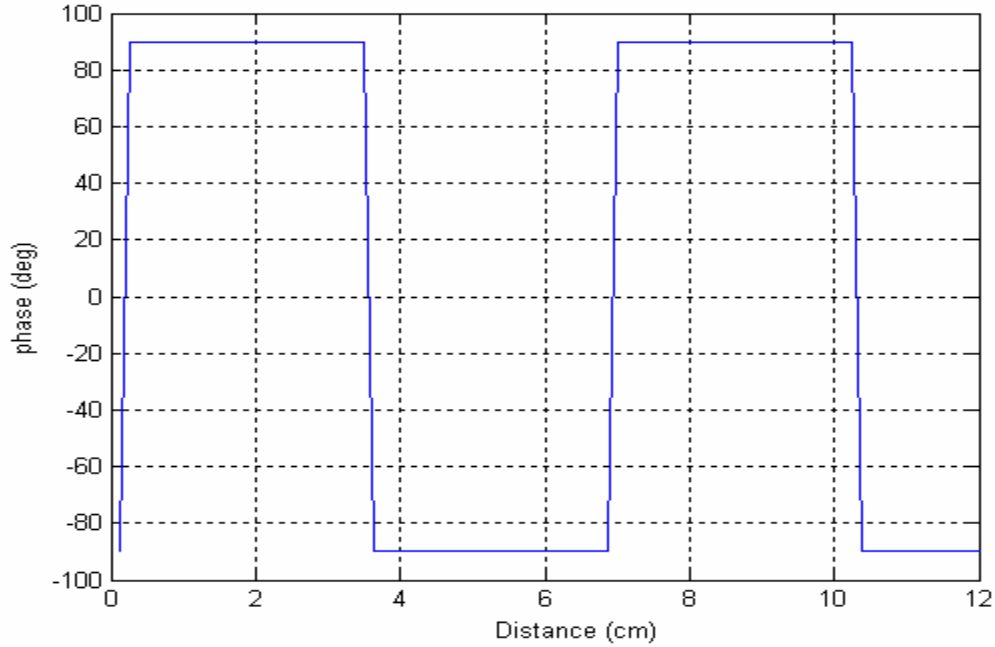

Figure 5-21: Density gradient phase along the length of the tube using the microphone method at $145.4\,dB$.

The reflection coefficient is obtained from the two-microphone method as discussed in Chapter 2. The magnitude and phase of the density gradient at various

locations of the impedance tube are calculated using Equation 5-5 and Equation 5-6 and are plotted in Figure 5-20 and Figure 5-21, respectively. From Figure 5-21, the phase at the reference microphone location was found to be -89.6^0 and used to obtain the phase angle from the deflectometer method relative to the specimen location $(d = 0)$.

5.3.3 Comparison of Results Obtained by the Two Methods

The amplitude of the density gradients obtained using the two methods is plotted with the uncertainty estimates (see uncertainty analysis in Appendix-C), in Figure 5-22 and Figure 5-23 at 145.4 dB and 126.4 dB respectively.

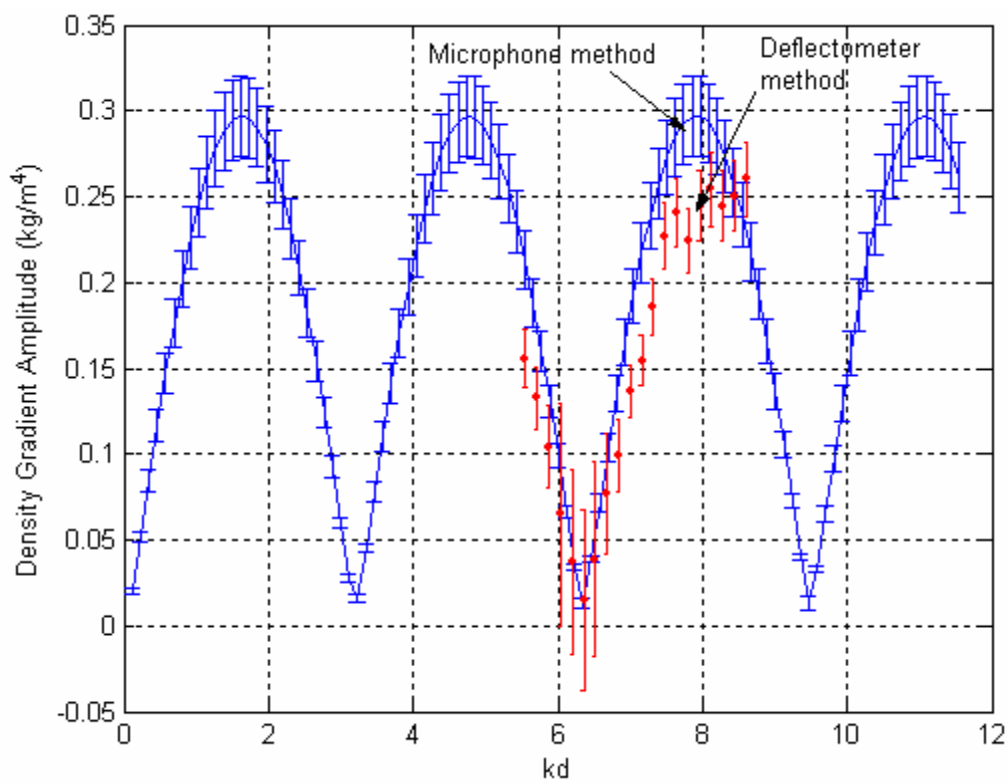

Figure 5-22: Magnitude of the density gradient using the two methods at 145.4 dB.

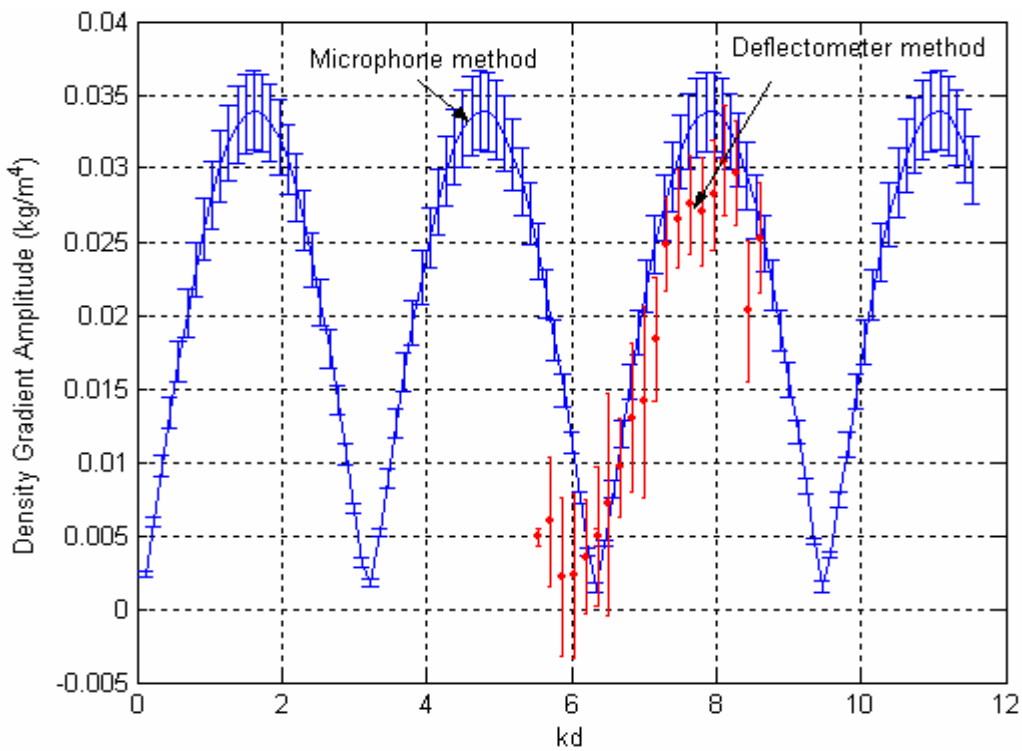

Figure 5-23: Magnitude of the density gradient using the two methods at $126.4\,dB$.

It can be seen that at higher SPL, the density gradient fluctuations obtained from the two methods are very similar. The deflectometer result deviated from the microphone method near the maxima of the density gradient. For the higher SPL, the estimates were close but did not overlap near the maxima. The most dominant term in the uncertainty estimate was the error due to the frequency response function and this error is dependent on the coherence. Interestingly, the agreement at the node is better than at the anti-node.

In the case of the lower SPL, the results obtained with the schlieren method had similar results and agreement as at higher SPL. The error in the density gradient field was larger and this is caused due to the lower coherence between the signals. The error bars were found to fall within the range of each other.

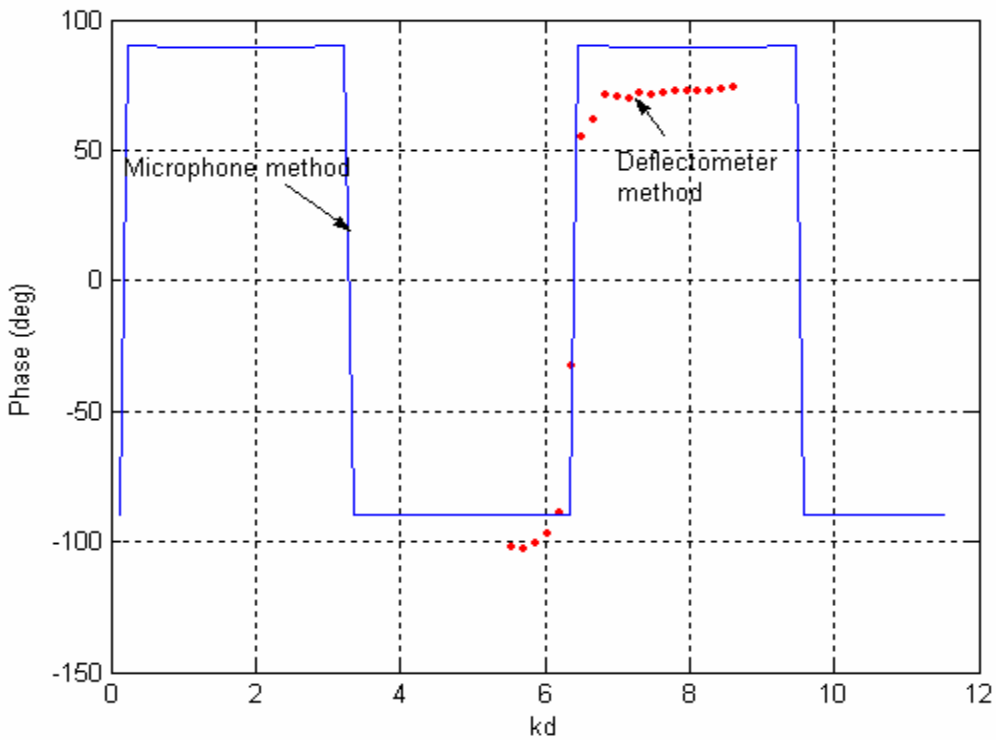

Figure 5-24: Phase of the density gradient using the two methods at 145.4 dB .

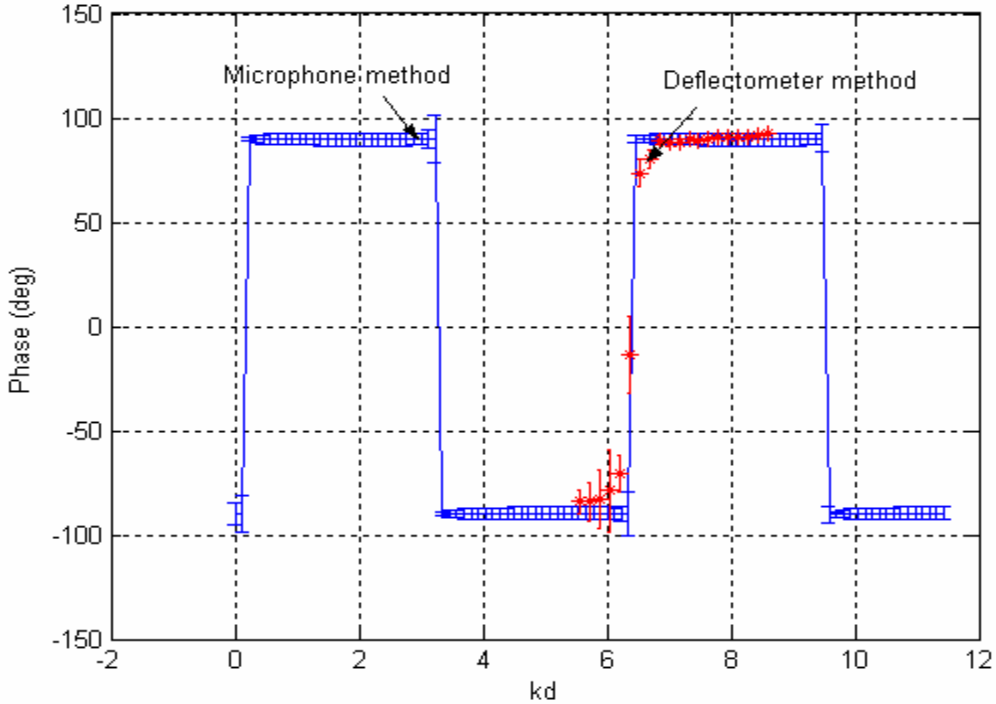

Figure 5-25: Phase of the density gradient using the two methods at 145.4 dB after the phase correction from the photo detector.

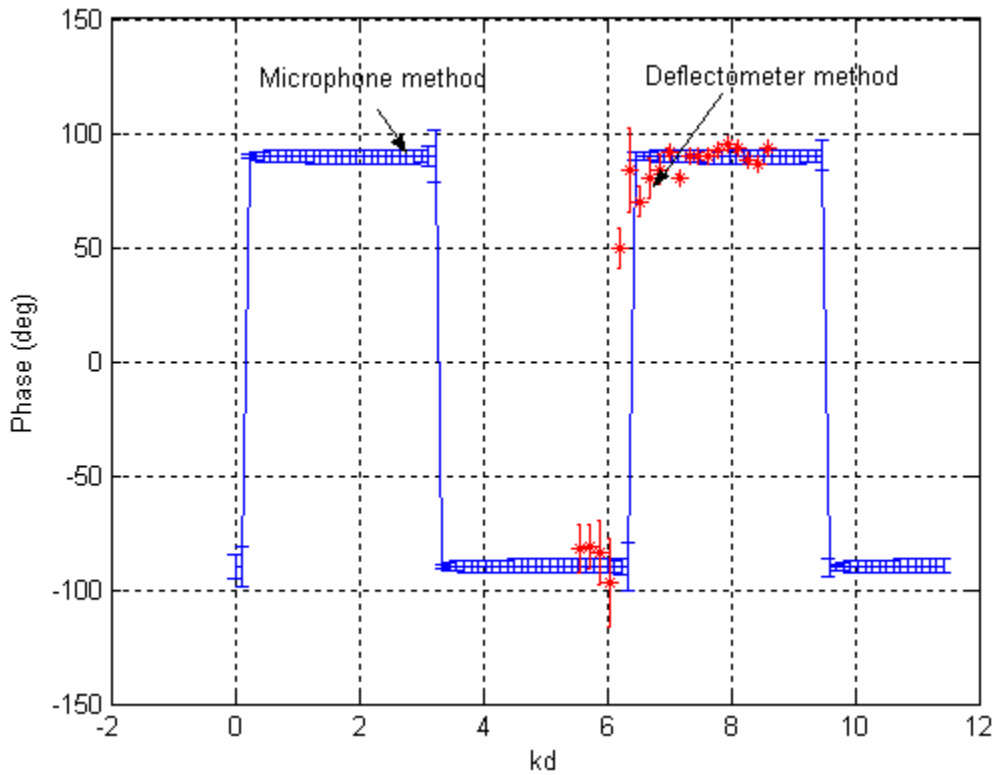

Figure 5-26: Phase of the density gradient using the two methods at 126.4 dB after the phase correction from the photo detector.

The phase distribution obtained from the two experimental techniques is compared in Figure 5-24. The reference microphone phase was calculated at 6.4 cm and added to the phase of the FRF to obtain the phase of the density gradient.

The result obtained from the optical method differed from the microphone method by a finite value. This shift was caused by the phase lag in the photo detector and was corrected via the dynamic calibration described in Section 4.3. Figure 5-25 and Figure 5-26 shows the corrected values of the phase with the error bars. They are found to fall well within the range of each other.

CHAPTER 6
CONCLUSION AND FUTURE WORK

This chapter summarizes the work done during the course of this project. Future work required to improve the overall performance of the instrument is discussed in the latter part of this chapter.

6.1 Conclusions

The ultimate objective of the research activity was to device a technique to visualize and measure the acoustic field in a normal acoustic impedance tube. A schlieren technique used for visualizing compressible flow was extended to measure the one-dimensional acoustic field with a much smaller density gradient. The instrument successfully detected density gradient fluctuations and data was obtained for sound pressure levels ranging from $123-157\ dB$. The amplitude and phase distributions of the density gradient were measured using the deflectometer. A second method based on the two-microphone method was used to verify the results. The results were in fairly good agreement except at the antinodes of the density gradient distribution. The discrepancy in the results can partially be explained using the uncertainty estimation.

6.2 Future Work

The study conducted provides rudimentary results, which can be used as a basis to study the behavior of an acoustic field in a normal acoustic impedance tube. The optical deflectometer system can be improved to obtain better results. The results of the detailed sensitivity analysis were obtained after the experiments. These results can be used to design a more sensitive instrument.

The system field of view is limited by the diameter of the lens/mirror, such that only a limited field of view could be obtained. Hence a larger diameter lens/mirror is required to visualize flow at lower frequencies.

Various types of spherical and achromatic aberrations were encountered using the lens-based system. Hence, a mirror-based system is highly recommended. Though the f number of the condenser lens and that of the first schlieren lens or mirror are shown to be equal in the ray diagram, it is advisable to have the f number of the condenser lens to be 1.5 to 2 times smaller [4]. This avoids non-paraxial effects caused by the condenser lens and also the effects of the reduced illumination of the light beam in the periphery.

Amplitude and phase mismatches were not corrected using the microphone switching method [25] for different values of SPL while the experiments were being conducted. This can be avoided by implementing the switching technique prior or during the test. The photo-detectors were characterized as over damped second order system after the completion of the experiments. A more sensitive photo-detector with lower noise and increased bandwidth, such as a cooled photo-multiplier tube should be used in future work.

Finally, using suitable boundary conditions, the pressure field can be obtained from the density gradient fluctuations by developing a suitable procedure. The technique can thus be extended to determine two- dimensional fields and can be used in the study of scattering effects. Also, the technique can now be extended to focused schlieren for the characterization of various specimens using the normal impedance tube.

APPENDIX A
KNIFE-EDGE GEOMETRY

The magnification between the focus of Lens 2 and the screen can be derived as follows.

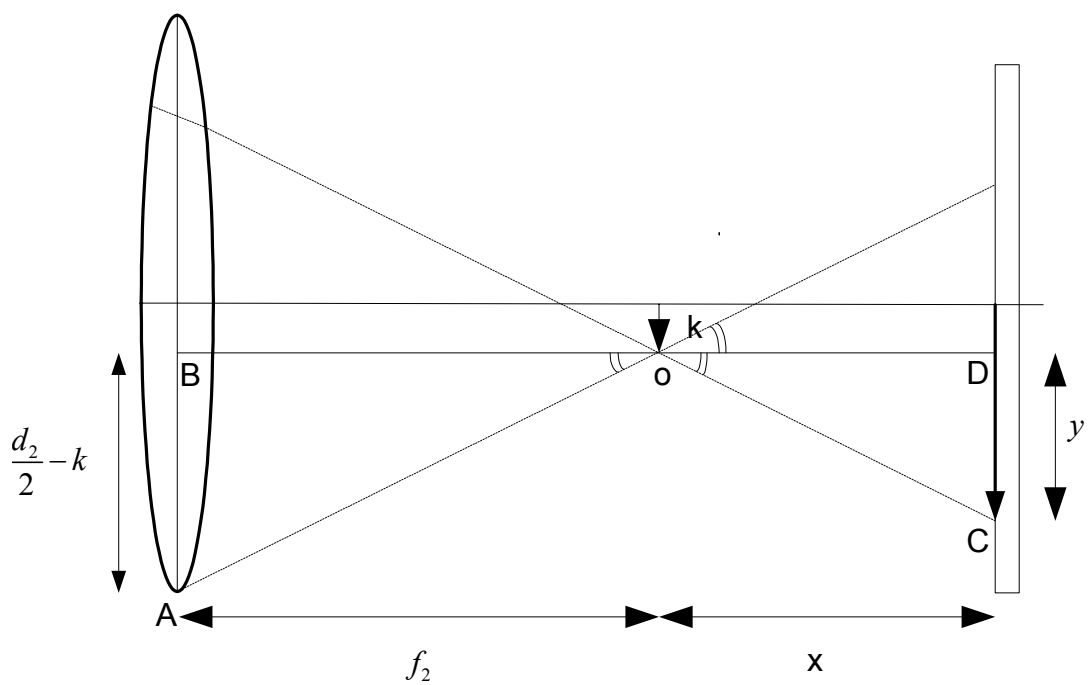

Figure A-1: Magnification of the source on the screen.

The Figure shows the region between the schlieren head and the screen (Figure 2-3) in the setup with the extreme rays originating from the top of the object. The image has a height k at the focus of Lens 2 and $y + k$ on the screen. It can be seen from Figure A-1 that $\angle AOB = \angle COD$. Hence

$$y = \frac{\frac{d_2}{2} - k}{f_2} x, \tag{1}$$

Magnification

$$m_3 = \frac{y + k}{k} = \frac{y}{k} + 1. \tag{2}$$

Substituting Equation A1 in Equation A3

$$m_3 = \frac{\frac{d_2}{2} - k}{k f_2} x + 1 \tag{3}$$

The total magnification at focus of Lens 2 is equal to $m_1 * m_2$ is

$$\frac{\infty}{f_1} \frac{f_2}{\infty} = \frac{f_2}{f_1}. \tag{4}$$

Therefore we have $k = \frac{f_2}{f_1} h$. Substituting in the Equation A3

$$m_3 = \frac{\frac{d_2}{2} - \frac{f_2}{f_1} h}{\frac{f_2^{\,2}}{f_1} h} x + 1. \tag{5}$$

APPENDIX B
LIGHT RAYS IN AN INHOMOGENEOUS FLUID

The derivation is done under the assumption that physical phenomena like diffraction or dispersion does not exist.

The refractive index is assumed to vary as a function of the three spatial coordinates.

$$n = n(x, y, z). \tag{B1}$$

The incident ray is initially parallel to the direction. According to the Ferment's principle, the variation of optical path length along a light ray in the refractive field must vanish.

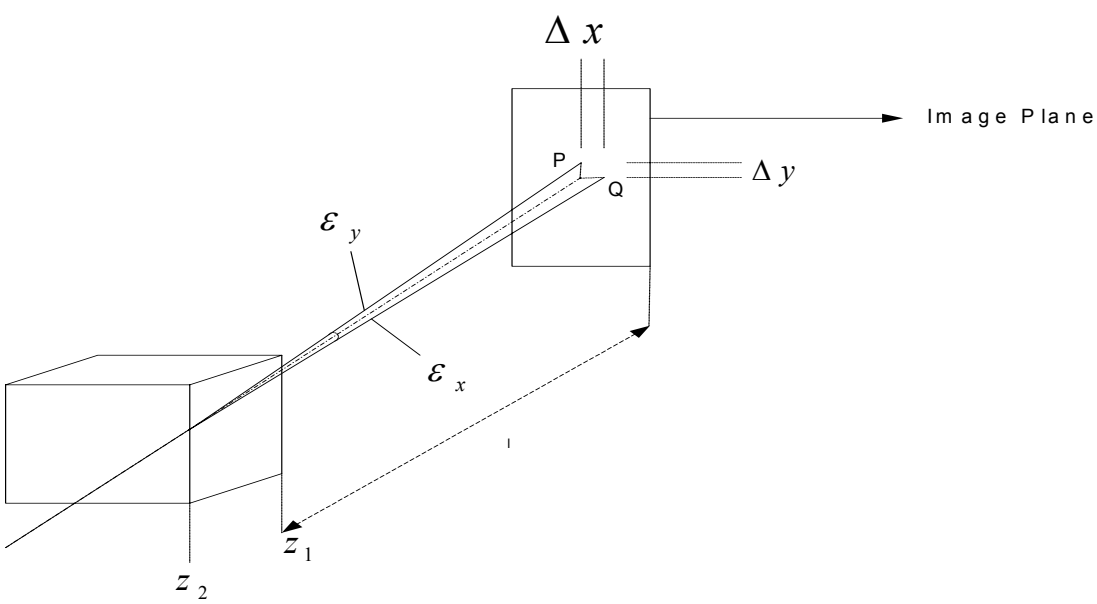

Figure B-1: Deflection of a light ray in inhomogeneous test object.

$$\delta \int n(x, y, z) ds = 0, \tag{B2}$$

where s denotes the arc length along the ray and

$$ds^2 = dx^2 + dy^2 + dz^2. \tag{B3}$$

Equation B2 is equivalent to two sets of differential equations

$$\frac{d^2x}{dz^2} = \left\{1 + \left(\frac{dx}{dz}\right)^2 + \left(\frac{dy}{dz}\right)^2\right\}\left\{\frac{1}{n}\frac{\partial n}{\partial x} - \frac{dx}{dz}\frac{1}{n}\frac{\partial n}{\partial z}\right\}, \tag{B4}$$

$$\frac{d^2y}{dz^2} = \left\{1 + \left(\frac{dx}{dz}\right)^2 + \left(\frac{dy}{dz}\right)^2\right\}\left\{\frac{1}{n}\frac{\partial n}{\partial y} - \frac{dy}{dz}\frac{1}{n}\frac{\partial n}{\partial z}\right\}. \tag{B5}$$

Assuming that the slopes of the ray $\frac{dx}{dz}$ and $\frac{dy}{dz}$ are very small as compared to unity and assuming $\frac{\partial n}{\partial x}$ and $\frac{\partial n}{\partial y}$ are of same order of magnitude Equation B4 and Equation B5 simplifies to

$$\frac{d^2x}{dz^2} = \frac{1}{n}\frac{\partial n}{\partial x}; \tag{B6}$$

$$\frac{d^2y}{dz^2} = \frac{1}{n}\frac{\partial n}{\partial y}. \tag{B7}$$

APPENDIX C
UNCERTAINTY ANALYSIS

This section estimates the error in both magnitude and phase of the density gradients measured using the deflectometer and the two-microphone method. The analysis uses a technique that employs a first order uncertainty estimate. For the uncertainty analysis of the microphone method, the technique is extended to complex variables [23]. The uncertainties in the individual variables are propagated through the data reduction equation into the result.

For a general case [24] if is a function of measured variables,

$$R = R(X_1, X_2, ...X_J). \tag{C1}$$

The uncertainty in the result is given by

$$U_r^2 = \left(\frac{\partial R}{\partial X_1}\right) U_{X_1}^2 + \left(\frac{\partial R}{\partial X_2}\right) U_{X_2}^2 + ... + \left(\frac{\partial R}{\partial X_J}\right) U_{X_J}^2, \tag{C2}$$

where U_{x_i} is the uncertainty in variable X_i. The partial derivative $\frac{\partial R}{\partial X_i}$ is defined as the sensitivity coefficient.

C.1 Uncertainty in Amplitude

C.1.1 Deflectometer Method

The data reduction procedure explained in section (5.3.2) is followed and a final expression for density gradient is derived as shown below.

The equations for $\Delta\Phi$ (Equation 4-16) and the slope of the calibration curve (Equation 4-17) were derived in section (4.1.1). Substituting, Equation 4-16 in Equation 4-17 we obtain the expression for Δa as

$$\Delta a(d) = \frac{|V'(d)|}{slope(d) \times (V_{ref\_DC}(d) - V_{ref\_dark})}. \tag{C3}$$

Substituting Equation C3 into Equation 2-29, we obtain the angular deflection as

$$\varepsilon_x(d) = \frac{|V'(d)|}{slope(d) \times f_2 \times (V_{ref\_DC}(d) - V_{ref\_dark})}. \tag{C4}$$

Subsequently, the density gradient is obtained by substituting Equation C4 in Equation 4-1 as

$$\left|\frac{\partial \rho}{\partial x}(d)\right| = \frac{|H|\sqrt{2G_{11}}}{slope(d) \times f_2 \times (V_{ref\_DC}(d) - V_{ref\_dark}) \times K \times W}, \tag{C5}$$

where G_{11} is the power spectrum of the input microphone signal at the operating frequency. The numerator essentially gives the voltage amplitude as a product of the magnitude of the frequency response function and the reference pressure amplitude. The density gradient can be written in the form of Equation C1 as a function of various parameters as shown

$$\left|\frac{\partial \rho}{\partial x}(d)\right| = \frac{\partial \rho}{\partial x}(|H(d)|, G_{11}, slope(d), f_2, V_{ref\_DC}(d), V_{ref\_dark}, W). \tag{C6}$$

Representing $\left|\frac{\partial \rho}{\partial x}\right|$ as $\rho_x^{'}$, various sensitivity coefficients can be written as follows.

$$\frac{\partial \rho_x^{'}}{\partial |H|} = \frac{\sqrt{2G_{11}}}{slope \times f_2 \times (V_{ref\_DC} - V_{ref\_dark}) \times K \times W}; \tag{C7}$$

$$\frac{\partial \rho_x^{'}}{\partial G_{11}} = \frac{|H|}{slope \times \sqrt{2G_{11}} \times f_2 \times (V_{ref\_DC} - V_{ref\_dark}) \times K \times W}; \tag{C8}$$

$$\frac{\partial \rho_x^{'}}{\partial slope} = -\frac{|H|\sqrt{2G_{11}}}{slope^2 \times \sqrt{2G_{11}} \times f_2 \times (V_{ref\_DC} - V_{ref\_dark}) \times K \times W}; \tag{C9}$$

$$\frac{\partial \rho_x^{'}}{\partial f_2} = -\frac{|H|\sqrt{2G_{11}}}{slope \times f_2^{\,2} \times (V_{ref\_DC} - V_{ref\_dark}) \times K \times W}; \tag{C10}$$

$$\frac{\partial \rho_x^{'}}{\partial V_{ref\_DC}} = -\frac{|H|\sqrt{2G_{11}}}{slope \times f_2 \times (V_{ref\_DC} - V_{ref\_dark})^2 \times K \times W}; \tag{C11}$$

$$\frac{\partial \rho_x^{'}}{\partial V_{ref\_dark}} = \frac{|H|\sqrt{2G_{11}}}{slope \times f_2 \times (V_{ref\_DC} - V_{ref\_dark})^2 \times K \times W}; \tag{C12}$$

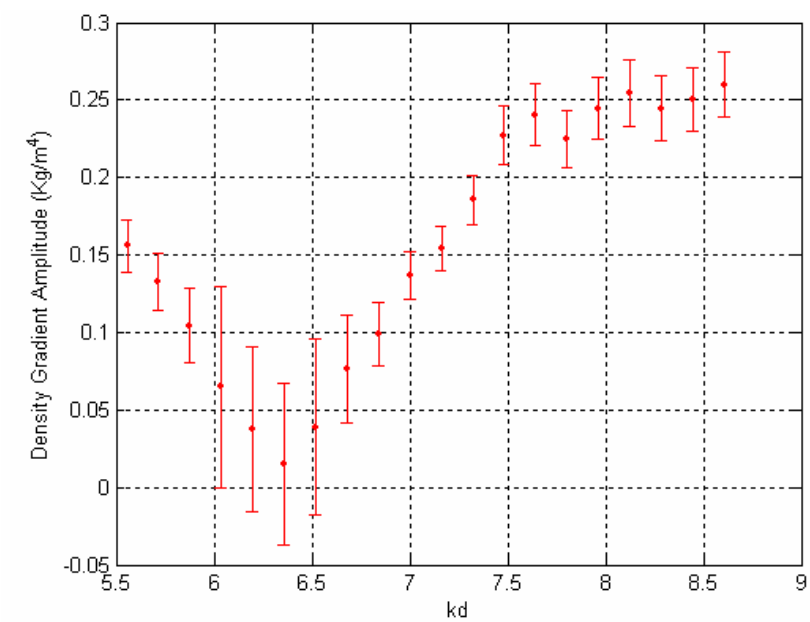

Figure C-1: Error bar in the amplitude of the density gradient using the deflectometer at 145.4 dB.

$$\frac{\partial \rho_x^{'}}{\partial W} = -\frac{|H|\sqrt{2G_{11}}}{slope \times f_2 \times (V_{ref\_DC} - V_{ref\_dark}) \times K \times W^2}; \tag{C13}$$

The uncertainties [19] U_{X_1} in H and G_{11} were $\frac{\sqrt{1-\gamma^2}}{|\gamma|\sqrt{2n}}$ and $\frac{1}{\sqrt{n}}$ respectively, where γ is the coherence and n is the number of averages. The remaining parameters were determined from the instrument specifications. Finally the total uncertainty in the density gradient was computed at each of the twenty locations and plotted in Figure C-1 for a SPL of 145.4 dB. The uncertainties in various parameters have been tabulated in C-1.

Table C-1: Uncertainties in various parameters for a deflectometer.

Parameter	U_{x_i}
$\|H\|$	$\frac{\sqrt{1-\gamma^2}}{\|\gamma\|\sqrt{2n}}$
G_{11}	$\frac{1}{\sqrt{n}}$
$slope$	95% error from the calibration curve
f_2	$8\,mm$
V_{ref_DC}	$0.6\,mV$
V_{ref_dark}	$0.6\,mV$
W	$0.0254\,mm$

C.1.1 Two Microphone Method

A similar approach was also followed for the two-microphone method. The expression for the absolute pressure in the normal acoustic impedance tube is derived in Equation 5-4. The constant A can be expressed as

$$A = \frac{\sqrt{(2G_{11})}}{\sqrt{(\cos(k(d1-l)) + |R|\cos(\phi_r - kd1 - kl))^2 + (\sin(k(d1-l)) + |R|\sin(\phi_r - kd1 - kl))^2}}. \quad \text{(C14)}$$

The expression for density gradient has already been derived in Equation 2-15 as

$$\frac{\partial \rho}{\partial x}(d) = \frac{Aike^{-ikl}(e^{ikd} - |R|e^{i\phi_r}e^{-ikd})}{c^2}.$$

It can be written as a function of four parameters as shown

$$\left|\frac{\partial \rho}{\partial x}(d)\right| = \frac{\partial \rho}{\partial x}(A(d1, l, G_{11}), l, |R|, \phi_r). \quad \text{(C15)}$$

Various sensitivity coefficients are calculated as follows

$$\frac{\partial \rho_x^{'}}{\partial A} = \frac{ike^{-ikl}(e^{ikd} - |R|e^{i\phi_r}e^{-ikd})}{c^2}; \quad \text{(C16)}$$

$$\frac{\partial \rho_x^{'}}{\partial |R|} = \frac{-Aike^{-ikl}|R|e^{i\phi_r}e^{-ikd}}{c^2}; \quad \text{(C17)}$$

$$\frac{\partial \rho_x^{'}}{\partial l} = \frac{Ak^2e^{-ikl}(e^{ikd} - |R|e^{i\phi_r}e^{-ikd})}{c^2}; \quad \text{(C18)}$$

$$\frac{\partial \rho_x^{'}}{\partial \phi_r} = \frac{Ake^{-ikl}|R|e^{i\phi_r}e^{-ikd}}{c^2}; \quad \text{(C19)}$$

It can be seen from Equation C14 that the constant A itself is a function of d_1

$$A = A(d1, l, G_{11}) \quad \text{(C20)}$$

And partial derivatives are given as

$$\frac{\partial A}{\partial G_{11}} = \frac{1}{\sqrt{(2G_{11})}\sqrt{(\cos(k(d1-l)) + |R|\cos(\phi_r - kd1 - kl))^2 + (\sin(k(d1-l)) + |R|\sin(\phi_r - kd1 - kl))^2}}; \tag{C21}$$

$$\frac{\partial A}{\partial l} = 0; \tag{C22}$$

$$\frac{\partial A}{\partial d1} = \frac{-A^3 |R| \sin(\phi_r - 2kd1)}{2G_{11}}; \tag{C23}$$

Table C-2: Uncertainties in various parameters for the microphone method.

Parameter	U_{x_i}
$\lvert R \rvert$	0.03
G_{11}	$\frac{1}{\sqrt{n}}$
l	$0.025\,mm$
d_1	$0.025\,mm$
ϕ_r	0.015

The uncertainty in A is

$$U_r^2 = \left(\frac{\partial A}{\partial l}\right) U_l^2 + \left(\frac{\partial A}{\partial G_{11}}\right) U_{G_{11}}^2 + \left(\frac{\partial A}{\partial d1}\right) U_{d1}^2. \tag{C24}$$

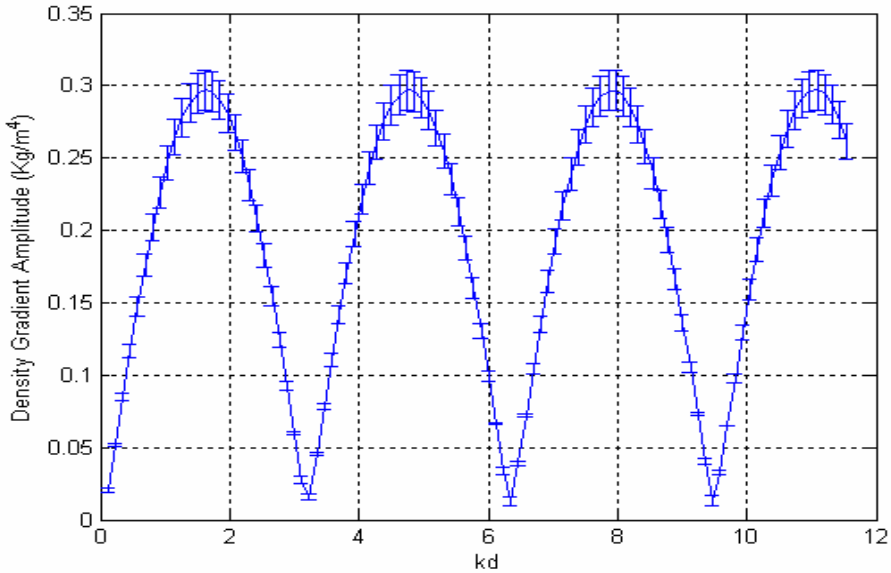

Figure C-2: Error bar in the amplitude using the microphone method 145.4 *dB* .

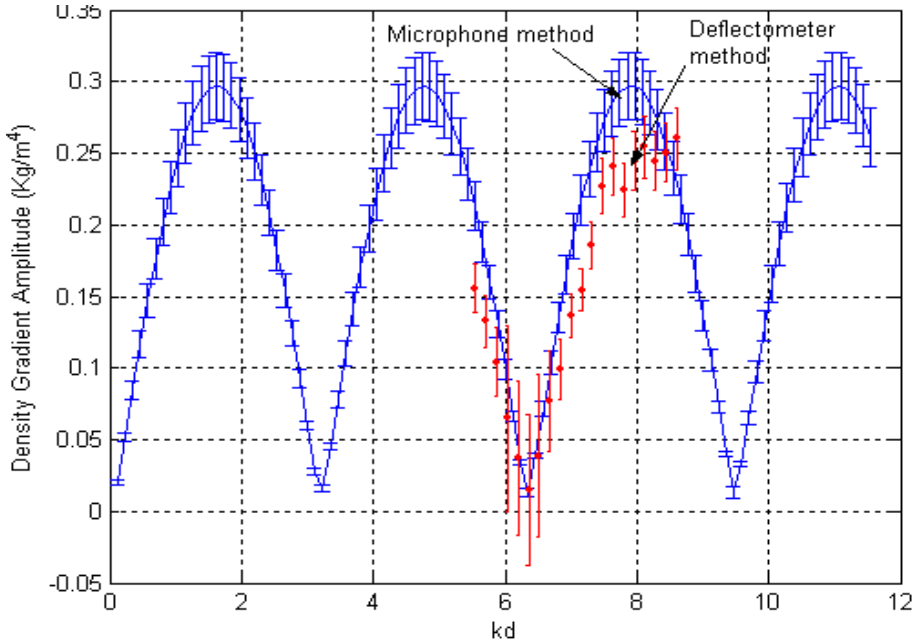

Figure C-3: Comparison of microphone and deflectometer method at 145.4 *dB* .

The uncertainty in $|R|$ and ϕ_r were calculated using the method of Schultz et al. [23]. The total uncertainty in the magnitude of the density gradient is obtained [23] using the equation

$$U_{|\rho_x^{'}|} = \frac{1}{|\rho_x^{'}|}\sqrt{\left[\mathrm{Re}(\rho_x^{'})\,\mathrm{Re}(U_{\rho_x^{'}})\right]^2 + \left[\mathrm{Im}(\rho_x^{'})\,\mathrm{Im}(U_{\rho_x^{'}})\right]^2} \tag{C25}$$

and plotted in Figure C-2.

In Figure C-3, the error bars obtained from the microphone method and the deflectometer method are compared. The uncertainties in various parameters are shown in Table C-2.

C.2 Uncertainty in Phase

C.2.1 Deflectometer Method

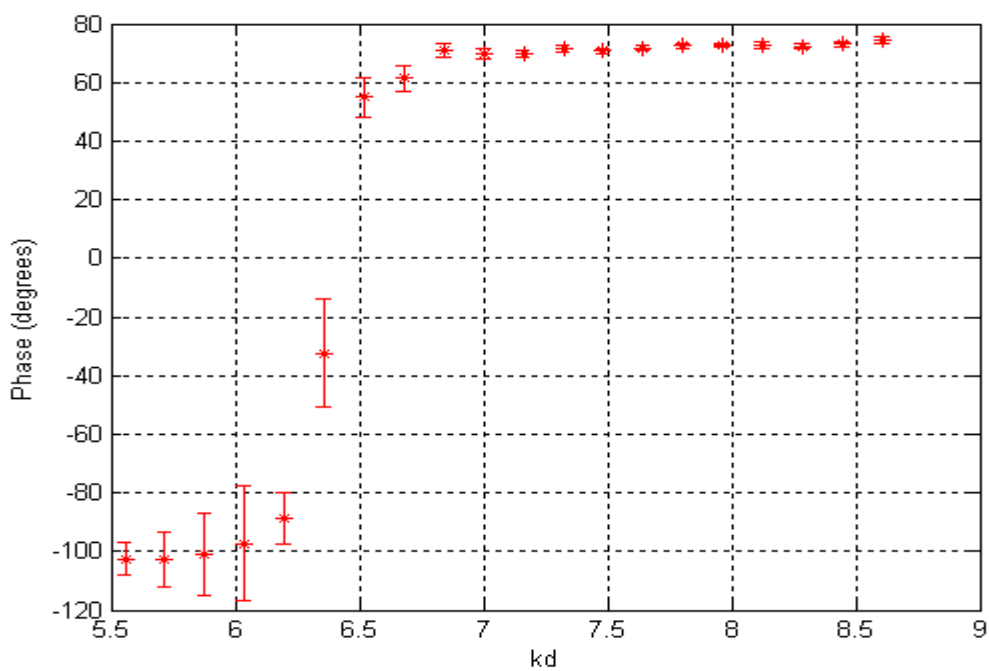

Figure C-4: Error bar in the phase using the deflectometer at 145.4 dB.

The phase of the density gradient using the deflectometer method is essentially the sum of the phase difference obtained from the frequency response function and the phase of the reference microphone at location d_1 as shown in Equation C26

$$\phi = \Theta + \tan^{-1}\left[\frac{\sin(k(d-l)) + |R|\sin(\phi_r - kd - kl)}{\cos(k(d-l)) + |R|\cos(\phi_r - kd - kl)}\right]. \tag{C26}$$

The uncertainty in Θ is given by [19] the expression $\frac{\sqrt{1-\gamma^2}}{|\gamma|\sqrt{2n}}$ and the uncertainty from the reference signal at d_1 is obtained from the two-microphone method.

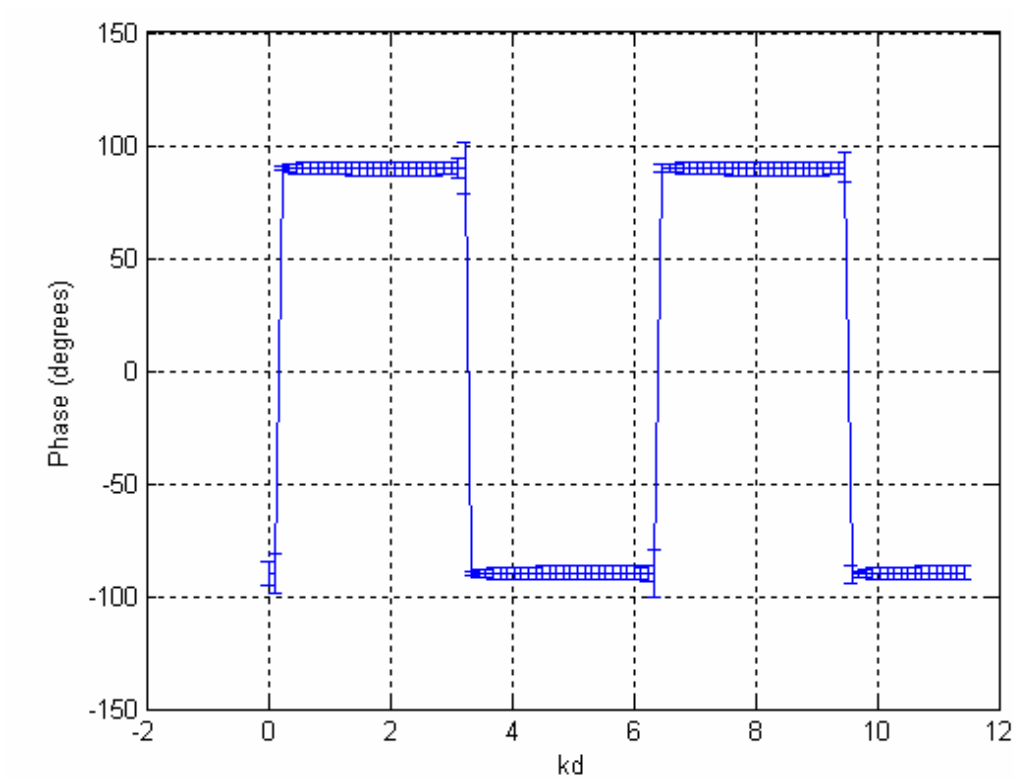

Figure C-6: Error bar in the amplitude using the deflectometer at 145.4 dB.

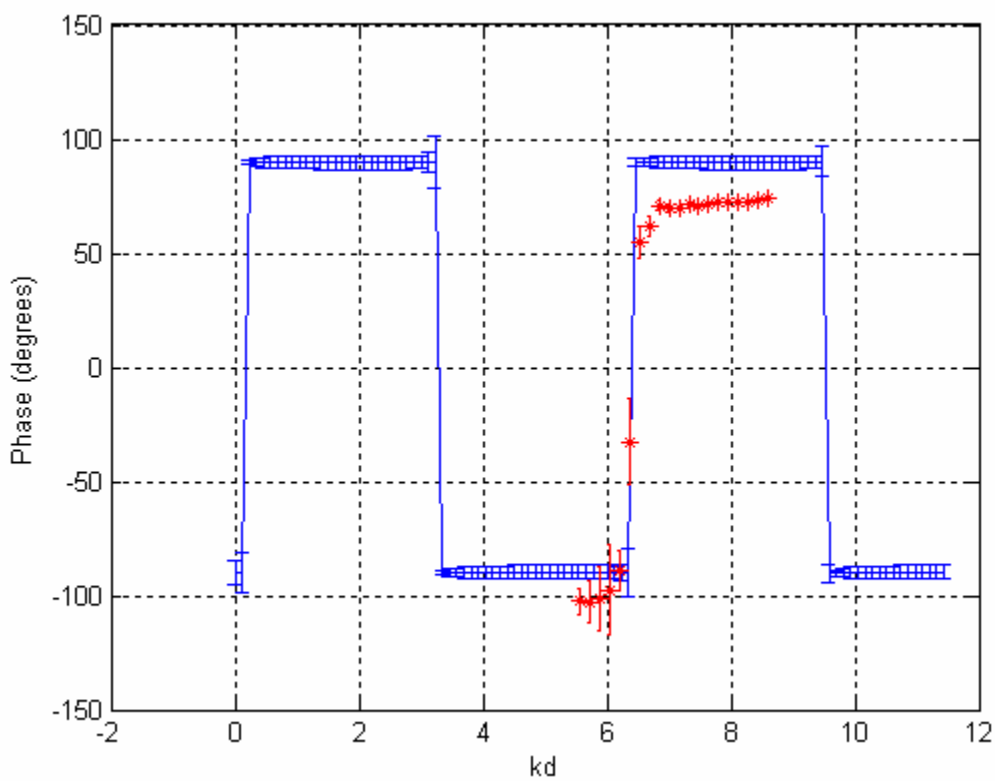

Figure C-7: Comparison of microphone and deflectometer method at 145.4 dB .

C.2.2 Microphone method

Procedure similar to Section C.1.2 was followed and the uncertainty in the phase is obtained [23] from the expression

$$U_{|\rho_x^{'}|} = \frac{1}{|\rho_x^{'}|^2}\sqrt{\left[\mathrm{Im}(\rho_x^{'})\,\mathrm{Re}(U_{\rho_x^{'}})\right]^2 + \left[\mathrm{Re}(\rho_x^{'})\,\mathrm{Im}(U_{\rho_x^{'}})\right]^2}. \qquad \text{(C27)}$$

The error bar has been plotted in Figure C-6 and the comparison in Figure C-7.

APPENDIX D
DENSITY GRADIENT

As discussed in Chapter 2 the pressure distribution in the impedance tube is given by

$$p(d) = (Ae^{-ikl}e^{ikd} + Be^{ikl}e^{-ikd}), \tag{D1}$$

where $p_i = Ae^{-ikl}$ and $p_r = Ae^{+ikl}$ and R defined as $R = \frac{p_r}{p_i}$

Equation D-2 can be expressed as

$$p(d) = Ae^{-ikl}(e^{ikd} + |R|e^{i\phi_r}e^{-ikd}). \tag{D2}$$

Using Equation 2-8, the pressure distribution can be con be converted into real and imaginary terms as

$$P(d) = A(\cos(k(d-l)) + i\sin(k(d-l)) + |R|\cos(\phi_r - kd - kl) + |R|i\sin(\phi_r - kd - kl)). \tag{D3}$$

The amplitude is given by

$$|p(d)| = A\sqrt{(\cos(k(d-l)) + |R|\cos(\phi_r - kd - kl))^2 + (\sin(k(d-l)) + |R|\sin(\phi_r - kd - kl))^2}. \tag{D4}$$

And the phase is given by

$$\psi(d) = \tan^{-1}\left[\frac{\sin(k(d-l)) + |R|\sin(\phi_r - kd - kl)}{\cos(k(d-l)) + |R|\cos(\phi_r - kd - kl)}\right].$$

The density gradient can be obtained from Equation 2-15 as

$$\frac{\partial \rho}{\partial x}(d) = \frac{Aike^{-ikl}(e^{ikd} - |R| e^{i\phi_r} e^{-ikd})}{c^2}.$$

It can be expressed as real and imaginary terms as

$$\frac{\partial \rho}{\partial x}(d) = \frac{Ak}{c^2}(i\cos(k(d-l)) - \sin(k(d-l)) - i|R|\cos(\phi_r - kd - kl) + |R|\sin(\phi_r - kd - kl)). \quad \text{(D4)}$$

The amplitude of Equation D-5 is given by

$$\left|\frac{\partial \rho}{\partial x}(d)\right| = \frac{Ak}{c^2}\sqrt{(\cos(k(d-l)) - |R|\cos(\phi_r - kd - kl))^2 + (-\sin(k(d-l)) + |R|\sin(\phi_r - kd - kl))^2}. \quad \text{(D6)}$$

And the phase is obtained from

$$\theta = \tan^{-1}\left[\frac{(\cos(k(d-l)) - |R|\cos(\phi_r - kd - kl))}{(-\sin(k(d-l)) + |R|\sin(\phi_r - kd - kl))}\right]. \quad \text{(D5)}$$

LIST OF REFERENCES

[1] **Merzkirch W** (1987) Flow visualization. 2nd edition, Academic Press, Inc., Orlando, FL.

[2] **Dyke V** Album of Fluid Motion, Parabolic Press, Incorporated, Stanford , California

[3] **Holder DW; North RJ** (1963) Schlieren Methods. National Physical Laboratory, Teddington, Middlesex.

[4] **Settles GS** (2001) Schlieren and Shadowgraph Techniques.ISBN 3-540-66155-7 Springer-Verlag Berlin Heidelberg NewYork.

[5] **Coleman HW; Steele WG** (1999) Experimentation and Uncertainity Analysis for Engineers, 2nd ed. New York: John Wiley & Sons, Inc..

[6] **Davis MR** (1971) Measurements in a subsonic turbulent jet using a quantitative schlieren technique. J.Fluid Mech (1971), vol. 46, part4, pp. 631-656.

[7] **Wilson LN; Damkevala RJ** (1969) Statistical Properties of Turbulent Density Fluctuations. J.Fluid Mech,vol. 43, part 2, pp. 291-303.

[8] **Davis MR** (1972) Quantitative schlieren measurement in a supersonic turbulent jet. J.Fluid Mech. (1972), vol. 51, part 3, pp. 435-447.

[9] **Davis MR** (1974) Intensity, Scale and Convection of Turbulent Density Fluctuations. J.Fluid Mech (1975), vol. 70, part 3, pp. 463-479.

[10] **Weinstein LM** (1991) An improved large-field focusing schlieren system. AIAA Paper 91-0567.

[11] **Alvi FS; Settles GS** (1993) A Sharp-Focusing Schlieren Optical Deflectometer. AIAA Paper 93-0629.

[12] **Weinstein LM** (1993) Schlieren system and method for moving objects. NASA CASE NO. LAR 15053-1.

[13] **Garg S; Settles GS** (1998) Measurements of a supersonic turbulent boundary layer by Focusing schlieren deflectometry. Experiments in Fluids 25 254-264.

[14] **Garg S; Cattafesta LN 111; Kegerise MA; Jones GS** (1998) Quantitative schlieren measurements of coherent structures in planar turbulent shear flows. Proc. 8th Int. Symp.Flow Vis, Sorrento, Italy.

[15] **Garg S; Cattafesta LN 111** (2000) Quantitative schlieren measurements of coherent structures in a cavity shear layer. Experiments in Fluids 30 pp. 123-124.

[16] **Michael A. Kegerise; Eric F. Spina; Louis N. Cattafesta 111** (1999) An Experimental Investigation of Flow-induced Cavity Oscillation. AIAA-99-3705.

[17] **Cattafesta LN; Kegerise ma; Jones GS** (1998) Experiments on Compressible Flow-Induced Cavity Oscillations. AIAA-98-2912.

[18] **Blackstock DT** (2000) Fundamentals of Physical Acoustics. New York: John Wiley & Sons, Inc.

[19] **ASTM-E1050-90**, "Impedance and Absorption of Acoustical Materials Using a Tube, Two Microphones, and a Digital Frequency Analysis System."

[20] **Ebert AF and Ross DF(1977)** "Experimental determination of acoustic properties using a two-microphone random-excitation technique" Journal of the Acoustical Society of America 61(5).

[21] **Bendat JS and Piersol AG** Random Data, 3rd ed. New York: John Wiley & Sons, Inc.

[22] **Taghavi R; Raman G**(1996) Visualization of supersonic jets using a phase conditioned focusing schlieren system. Experiments in Fluids 20 472-475

[23] **Settles GS** (2001) Schlieren and Shadowgraph Techniques. Visualizing Phenomena in Transparent Media.

[24] **Leonard M. Weinstein** (1991) Large-Field High-Brightness Focusing Schlieren System.AIAA Paper 91-0567

[25] **Schultz T; Louis N. Cattafesta 111; Nishida T; Sheplak M** (1998) Uncertainty Analysis of the Two-Microphone Method for Acoustic Impedence Testiong

[26] **Horowitz S; Nishida T; Cattafesta L N; Sheplak M** (2001) Compliant-Backplate Helmholtz Resonators for Active Noise Control Application, 39 th Aerospace Science Meeting & Exhibit, 2001

BIOGRAPHICAL SKETCH

Priya Narayanan was born in 1979 in Malappuram, Kerala, India. She moved to the State of Kuwait in 1981 and graduated from The Indian School in Salmiya, Kuwait in 1997. She went back to India for her Bachelors degree and obtained her Bachelor's of Technology degree in Aerospace Engineering from Indian Institute Of Technology, Madras, India in May 2001. She is currently pursuing her Master of Science degree in the Department of Mechanical and Aerospace Engineering at the University of Florida.